Geochemical Perspectives Letters

© 2023 The Authors
Published by the European Association of Geochemistry

Authigenic minerals reflect microbial control on pore waters in a ferruginous analogue

A. Vuillemin[1*], M. Morlock[2,3], A. Paskin[4], L.G. Benning[4,5], C. Henny[6], J. Kallmeyer[1], J.M. Russell[7], H. Vogel[2]

OPEN ACCESS

https://doi.org/10.7185/geochemlet.2339

Abstract

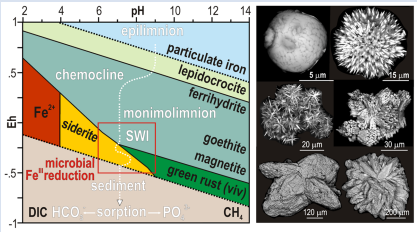

Ferruginous conditions prevailed in the oceans through much of Earth's history. However, minerals recording these conditions remain difficult to interpret in terms of biogeochemical processes prior to lithification. In Lake Towuti, Indonesia, ferruginous sediments are deposited under anoxic sulfate-poor conditions similar to the Proterozoic oceans, allowing the study of mineralogical (trans)formations during microbial diagenesis.

Comprehensive pore water geochemistry, high resolution geochemical core profiles, and electron microscopy of authigenic minerals revealed *in situ* formation of magnetite, millerite, and abundant siderite and vivianite along a 100 m long sequence. Framboidal magnetites represent primary pelagic precipitates, whereas millerite, a sulfide mineral often overlooked under sulfate-poor conditions, shows acicular aggregates entangled with siderite and vivianite resulting from saturated pore waters and continuous growth during burial. These phases act as biosignatures of microbial iron and sulfate reduction, fermentation and methanogenesis, processes clearly traceable in pore water profiles.

Variability in metal and organic substrates attests to environment driven processes, differentially sustaining microbial processes along the stratigraphy. Geochemical profiles resulting from microbial activity over 200 kyr after deposition provide constraints on the depth and age of mineral formation within ferruginous records.

Received 4 September 2023 | Accepted 7 November 2023 | Published 6 December 2023

Introduction

Ferruginous conditions (iron-rich, sulfate-poor) were widespread in the Archean and Proterozoic oceans and resulted in the deposition of ancient iron formations (Canfield *et al.*, 2008). Precambrian iron formations are composed of diverse iron oxides and carbonates thought to have formed as primary pelagic precipitates from the recrystallisation of ferric-ferrous iron (oxyhydr)oxides (Halevy *et al.*, 2017). Sulfides are also occasionally reported to occur, but only in minor quantities due to the scarcity of seawater sulfate at the time (Fakhraee *et al.*, 2019). Although the Proterozoic Earth was an essentially microbial world, mineral phases precipitated by microbial biogeochemical cycling of iron, sulfur and carbon remain poorly constrained in terms of early diagenetic imprints prior to sediment lithification (Posth *et al.*, 2014). Characterising and identifying such mineral phases is therefore paramount in order to employ their signatures as recorders of past ferruginous environments and as tracers of microbial processes of the Earth's early oceans (Tosca *et al.*, 2019).

Modern analogues to Earth's early oceans (Swanner *et al.*, 2020) that allow the study of both modern pore water geochemistry and short term diagenetic evolution of ferruginous sediments are scarce. One such environment is the ferruginous sediments deposited in the Malili Lakes (Russell *et al.*, 2016), a chain of five interconnected tectonic lakes hosted in variably weathered (ultra)mafic rocks on Sulawesi, Indonesia (Fig. 1a, b). Lateritic erosion of the catchment supplies considerable amounts of iron (oxyhydr)oxides, but little sulfate, to the lakes (Morlock *et al.*, 2018). Lake Towuti (2.5° S, 121° E), with a maximum water depth of *ca.* 200 m, is presently oxygen depleted below 130 m depth (Fig. 1c) displaying a persistent monimolimnion wherein primary ferric iron phases, mostly ferrihydrite ($Fe_2O_3 \cdot 0.5H_2O$), undergo reductive dissolution (Bauer *et al.*, 2020). Subsequent sediment (trans)formation during early diagenesis (Vuillemin *et al.*, 2019, 2020) precipitates secondary mineral phases, such as siderite ($FeCO_3$) and vivianite ($Fe_3[PO_4]_2 \cdot 8H_2O$). Geomicrobiological investigations have shown that iron-, sulfur- and methane-related biogeochemical processes coexist in Lake Towuti sediments (Vuillemin *et al.*,

1. GFZ German Research Centre for Geosciences, Section Geomicrobiology, Telegrafenberg, 14473 Potsdam, Germany
2. Institute of Geological Sciences and Oeschger Centre for Climate Change Research, University of Bern, Baltzerstrasse 1-3, 3012 Bern, Switzerland
3. Present address: Department of Ecology and Environmental Science, Umeå University, Linnaeus väg 6, 90187 Umeå, Sweden
4. GFZ German Research Centre for Geosciences, Section Interface Geochemistry, Telegrafenberg, 14473 Potsdam, Germany
5. Department of Earth Sciences, Free University of Berlin, 12249 Berlin, Germany
6. Research Center for Limnology and Water Resources, National Research and Innovation Agency (BRIN), Republic of Indonesia, Cibinong, 16911, Jawa Barat, Indonesia
7. Department of Earth, Environmental, and Planetary Sciences, Brown University, 324 Brook Street, Providence, RI, USA
* Corresponding author (email: aurele.vuillemin@gfz-potsdam.de)

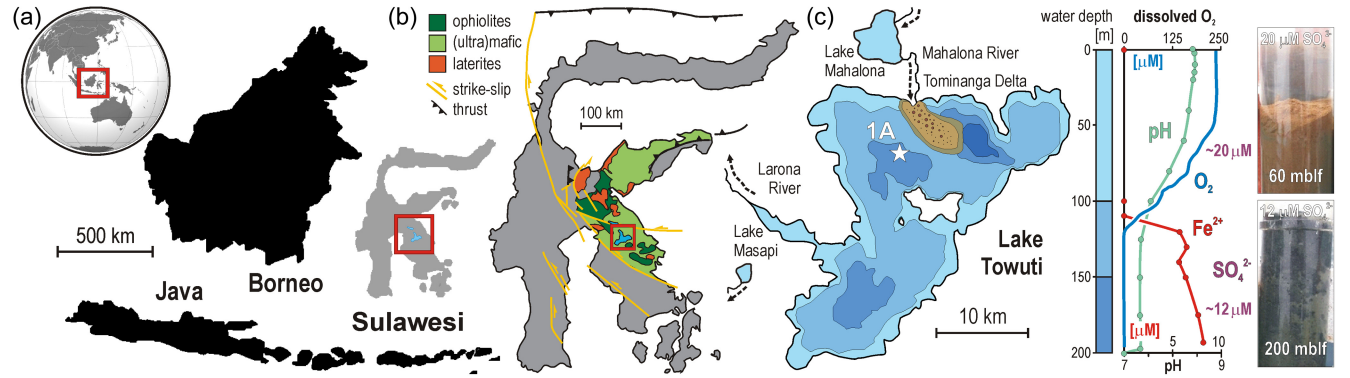

Figure 1 Site description of Lake Towuti. **(a)** World map displaying the location of Sulawesi Island, with close up on the Indonesia archipelago and location of the Malili Lake System. **(b)** Map of Sulawesi illustrating the (ultra)mafic and lateritic geology of the Malili Lake catchment. **(c)** Bathymetric map of Lake Towuti with position of drill site TDP-1A (156 m water depth), dissolved oxygen, iron, sulfate and pH profiles of Lake Towuti's water column (Bauer *et al.*, 2020), and gravity cores retrieved from 60 and 200 m water depth illustrating redox conditions at the water-sediment interface.

2016, 2018). Due to extremely low sulfate concentrations (<20 µM), sediment organic matter (OM) remineralisation proceeds mainly through methanogenesis (Friese *et al.*, 2021). These sedimentary conditions make Lake Towuti a unique ferruginous analogue in which to study the evolution of pore water geochemistry under the influence of microbial reduction and mineral (trans)formations prior to sediment lithification (Vuillemin *et al.*, 2023).

Here, we analyse one 100 m long sediment sequence to investigate the link between putative microbial processes and geochemical gradients under which authigenic minerals precipitate. We present detailed pore water geochemistry and high resolution geochemical core profiles down to a basal age of about ~1 Ma (Russell *et al.*, 2020). Using transmitted light and scanning electron microscopy (SEM), we illustrate characteristic authigenic mineral phases, namely magnetite (Fe_3O_4), millerite (NiS), siderite and vivianite, which occur in varying quantities throughout the stratigraphy. Together these data document the direct precipitation of successive phases from pore waters, highlight microbial processes of sediment remineralisation underlying reductive diagenesis, and allow us to establish mineral biosignatures in ferruginous records.

Methods

The Towuti Drilling Project (TDP) coring operations were carried out by the International Continental Scientific Drilling Program (ICDP) in spring-summer 2015, using the Deep Lakes Drilling System (Russell *et al.*, 2016). Hole TDP-1A (156 m water depth) was drilled with a contamination tracer to aid geomicrobiological sampling (Friese *et al.*, 2017). In the field, pristine core sections were transferred into an anaerobic chamber for pore water extraction, using Rhizon samplers for soft sediment, and an IODP-style titanium cylinder and hydraulic press for compact samples deeper than 10 m below lake floor (mblf). Alkalinity, pH, and Fe^{2+}, Mn^{2+} and PO_4^{3-} concentrations were determined *via* colorimetric titration, potentiometry and spectrophotometry, respectively. Dissolved inorganic carbon (DIC) was calculated by solving the carbonate system using the pH and alkalinity profiles and borehole temperatures. Major dissolved elements and volatile fatty acids (VFAs) were analysed by ion chromatography. Pore water trace metals were quantified by ICP-MS. Potential sulfate reduction rates (pSRRs) were determined by sediment incubation with radioactive $^{35}SO_4^{2-}$ (Friese *et al.*, 2021).

All cores from TDP site 1 were split and scanned at the National Lacustrine Core Facility (LacCore), described macroscopically and microscopically to determine their stratigraphy and composition. A composite core was established based on visual alignment of lithologic features and magnetic susceptibility measurements (Russell *et al.*, 2020). The upper 100 m of the composite cores were scanned at 5 mm resolution on an XRF core scanner (ITRAX, Cox Ltd.) equipped with chromium and molybdenum X-ray tubes to resolve high atomic mass elements (Morlock *et al.*, 2021). The remainder of core TDP-1A was subsampled for heavy mineral extraction (≥2.9 g cm^{-3}) *via* density and magnetic separation. Heavy mineral extracts were fixed onto SEM aluminium stubs and carbon coated (~20 nm layer), using a Leica EM ACE600 high vacuum sputter coater. Morphological investigation and elemental point analyses were performed on a Zeiss Ultra 55 Plus field SEM and FEI Quanta 3D FEG, both coupled to energy dispersive X-ray spectrometres (EDX). All methods are detailed in the Supplementary Information.

Results and Discussion

Authigenic mineral shapes and compositions can be employed to trace changes in redox controlled variations in water and pore fluid geochemistry associated with microbial processes in the upper sediment sequence. If mineral precipitation continues during burial, their signatures deviate from the stratigraphic context.

Pore water geochemical evolution and mineral precipitation. Reducible iron oxides in sediments originate from lateritic weathering of Towuti's (ultra)mafic catchment (Morlock *et al.*, 2018) and authigenic oxidation of ferrous iron in the water column (Sheppard *et al.*, 2019). Consequently, alternating red and green sediments reflect variations in the composition, abundance and changes in iron oxidation state through time (Russell *et al.*, 2020). During settling when the water column is stratified, particulate iron undergoes partial reductive dissolution in the monimolimnion (Bauer *et al.*, 2020), precipitating pelagic framboidal magnetites (Fig. 2a). Currently bottom waters contain *ca.* 20 to 12 µM sulfate (Vuillemin *et al.*, 2016), promoting sulfate reduction rates (SRR) that are highest at the sediment water interface (SWI) and drastically drop within the upper 20 cmblf (Fig. 3a). In contrast to euxinic conditions under which Fe sulfides (*e.g.*, mackinawite) act as the primary Ni-hosting phases (Mansor *et al.*, 2019), iron sulfides were not observed. Under the present ferruginous conditions, sulfate reduction with organic carbon as the reductant produces sulfide that reacts with nickel (Fig. 4) and precipitates millerite (NiS). The habits of millerites identified at 0.2 mblf and deeper suggest both pelagic

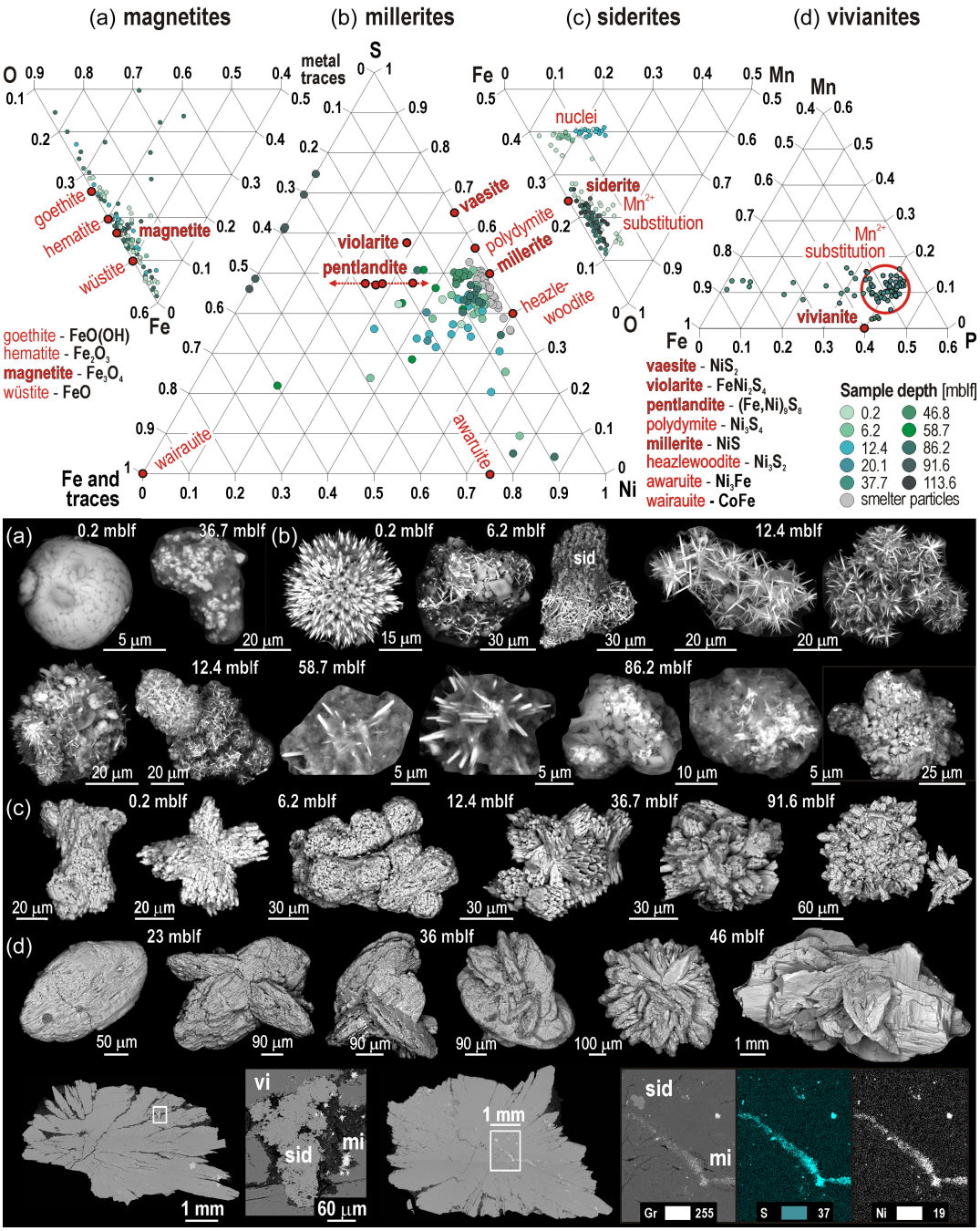

Figure 2 EDX point analyses and SEM images of diagenetic minerals. **(Top)** Ternary plots show: **(a)** magnetites and coextracted iron oxides (goethite, wüstite), **(b)** millerites with incorporation of Fe^{2+} traces, **(c)** siderites and **(d)** vivianites with substitution of Mn^{2+} for Fe^{2+}. Smelter particles represent airborne contaminants from the nearby mine. **(Bottom) (a)** Magnetites in framboidal habits; **(b)** millerites in acicular spherules and aggregates, sometimes entangled and overgrown by siderites; **(c)** siderites aggregating into twins and mosaic monocrystals; and **(d)** vivianites in tabular habit developing into rosettes. The crystal section shows inclusions of millerite and siderite.

precipitation and post-depositional growth at the SWI and in shallow sediments during active sulfate reduction (Fig. 2b).

Due to stratification in ferruginous Lake Towuti, the main terminal electron acceptors (*i.e.* O_2, NO_3^-, SO_4^{2-}) are rapidly depleted in the sediment (Figs. 1, 3a), which implies that anaerobic OM degradation should proceed *via* mineral ferric iron and CO_3^{2-} reduction. Reductive dissolution of hydrous ferric oxides (*e.g.*, ferrihydrite) continues in shallow sediments releasing substantial amounts of Fe^{2+} (278 µM) to the pore water (Fig. 3a). Below 50 cmblf, because goethite and magnetite represent the main reducible ferric phases remaining in sediments (Figs. 2a, S-1), fermentation is preferentially performed over microbial respiration of less reactive substances (Friese *et al.*, 2021). Nevertheless, steadily increasing metal concentrations in pore water (Mn, As, Co) suggests that Fe reduction concomitant with fermentation (Fig. 3a) continues at slow rates, promoting the dissolution of less reactive ferric-ferrous phases during burial.

From 1 to 10 mblf, pore water NH_4^+, PO_4^{3-} and VFA concentrations provide concomitant evidence of microbial OM degradation (Fig. 3a). Between 30 cmblf and 5 mblf, formate, lactate, acetate and butyrate concentrations vary with metabolic production and consumption (*i.e.* acidogenesis, acetogenesis). Below

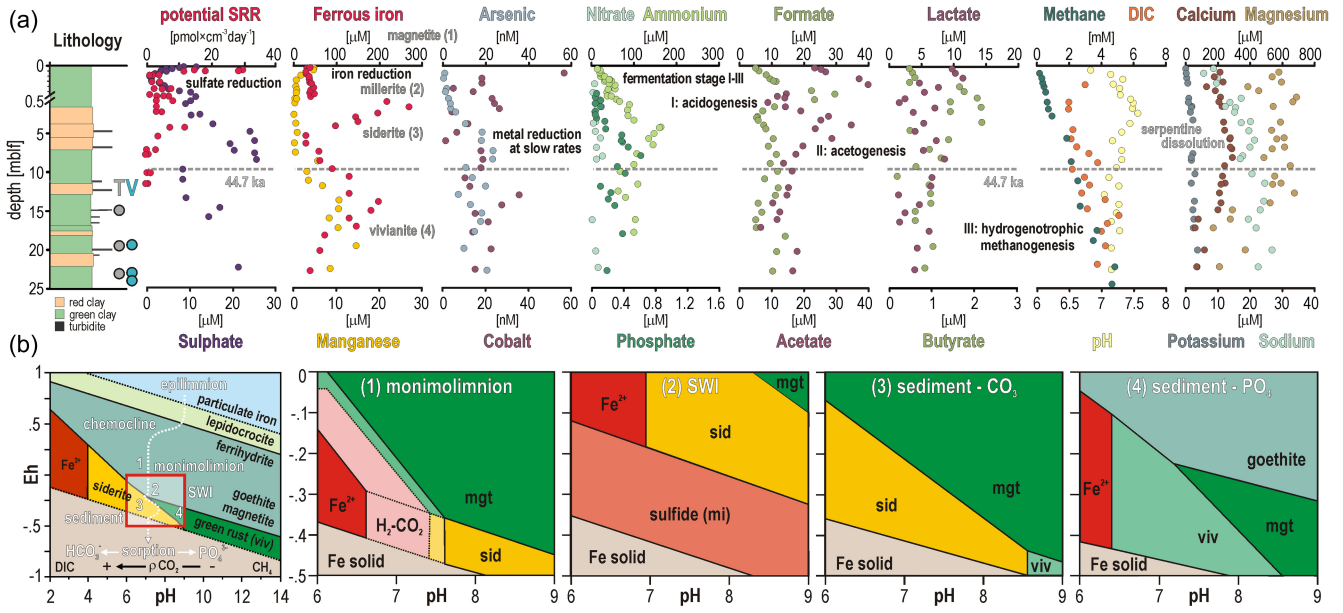

Figure 3 Depth profiles for pore water geochemistry and stability diagrams for Fe-bearing phases. **(a)** Lithology of Lake Towuti's upper 25 mblf including tephras (T) and vivianites (V); potential sulfate reduction rates (SRR); pore water concentrations for sulfate, ferrous iron, manganese, arsenic, cobalt, nitrate, ammonium, phosphate, formate, acetate, lactate, butyrate, methane, dissolved inorganic carbon (DIC), pore water pH, calcium, magnesium, potassium and sodium. Data points represent averaged triplicates (reproducibility <5 %). The dotted line signifies the base of the ^{14}C ages, *i.e.* 44.7 ka (Russell *et al.*, 2020). **(b)** Stability diagram tracing the measured pH and decreasing Eh during sedimentation and burial, successively focusing on conditions (red square) observed during *in vitro* microbial Fe^{3+} reduction (Maher *et al.*, 2003) corresponding to (1) the monimolimnion (Roh *et al.*, 2003), (2) sediment water interface (SWI) wherein millerite replaces pyrite (Craw and Bowell, 2014), (3) shallow and (4) deep sediments under carbonate- (Zachara *et al.*, 2002) and phosphate-saturated conditions (Morton and Edwards, 2005), respectively.

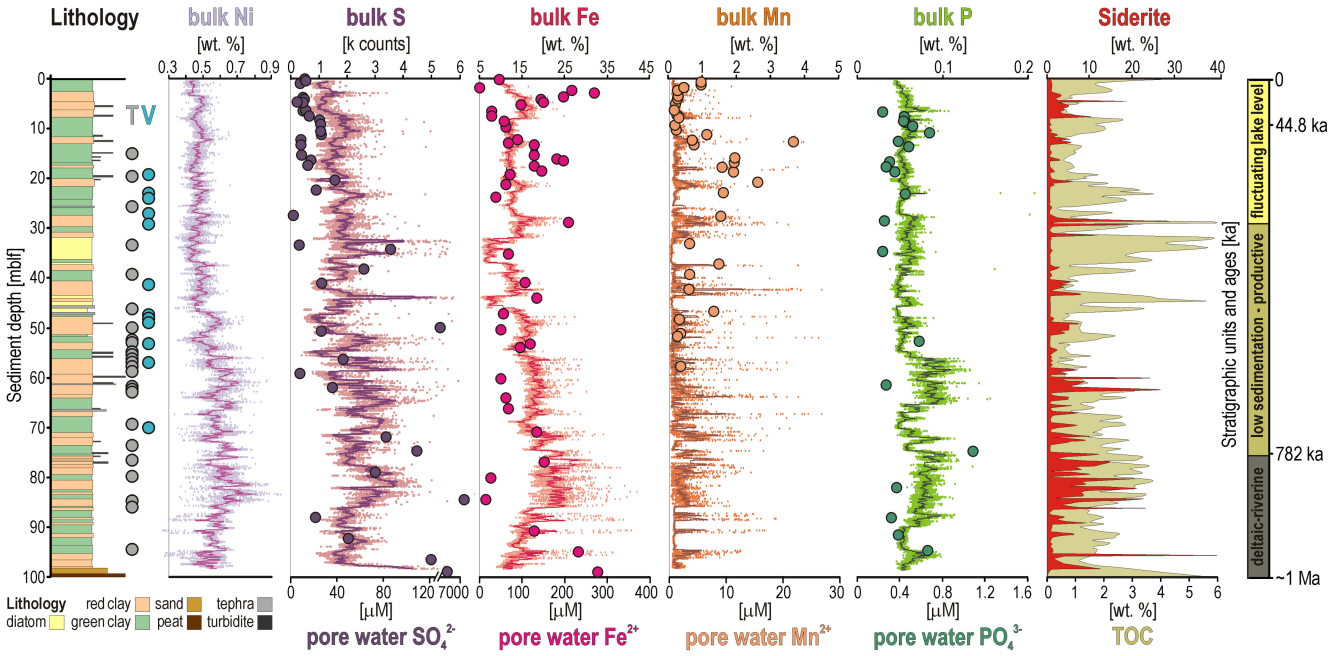

Figure 4 Depth profiles for bulk sediment, and pore water geochemistry. **(Left to right)** Stratigraphy of site TDP-1A with tephras (T) and vivianites (V); XRF core scanning profiles for Ni, S, Fe, Mn and P in bulk sediment overlain by pore water concentrations for SO_4^{2-}, Fe^{2+}, Mn^{2+} and PO_4^{3-}; siderite concentration based on coulometry; total organic carbon (TOC). XRF core scanning profiles represent point analyses with moving averages at 5 mm and 2 cm resolution, respectively. Data points represent averaged triplicates (reproducibility <5 %).

5 mblf, persistently low VFA concentrations (<20 µM) indicate complete remineralisation to methane (Friese *et al.*, 2021) accompanied by a decrease in microbial uptake of PO_4^{3-}. Such stepwise fermentation and steady increase in DIC delimit the depth at which pore waters reach siderite saturation (Vuillemin *et al.*, 2019). The pore water pH (7.1–7.5) implies that this biogenic DIC reacts in the form of HCO_3^- with dissolved Fe^{2+} to consistently precipitate siderite between 50 cmblf and 5 mblf

(Table S-1), whereas CO_2 fixation *via* hydrogenotrophic methanogenesis subsequently reduces DIC activity in pore waters (Fig. 3b).

The increasing pore water Na^+, Ca^{2+} and Mg^{2+} concentrations with depth (Fig. 3) indicate that (ultra)mafic sheet silicates (*e.g.*, serpentine) partially dissolve after burial (Table S-1). Ca^{2+} and Mg^{2+} concentrations are predicted to decrease the solubility of PO_4^{3-} in ferruginous solutions (Kubeneck *et al.*, 2023), thereby influencing pore water chemical equilibrium. Their presence in pore water could exert control over the onset of vivianite precipitation (Fig. 2d) after siderite (Vuillemin *et al.*, 2020). Ca^{2+} and Mg^{2+} concentrations drop around 15 mblf, suggesting that PO_4^{3-} supplants CO_3^{2-} for precipitation with Fe^{2+} and Mn^{2+} available in pore water (Fig. 3).

Pore water geochemical profiles in Lake Towuti's upper sediment column stem from microbial activity and dissolution-precipitation of specific mineral phases (Figs. 2, 3). We observe a characteristic succession of authigenic mineral precipitation as a function of chemical equilibration of ferruginous pore waters (Jiang and Tosca, 2019) during anaerobic respiration of terminal electron acceptors and sediment OM remineralisation. Namely, magnetite, millerite, siderite and vivianite represent biosignatures of microbial iron and sulfate reduction, fermentation and methanogenesis lasting 200 kyr after deposition.

Geochemical gradient and continuous mineral overgrowth. Based on the geochemical gradient that developed in Lake Towuti's upper 25 m of sediment (Fig. 3a) and pH-Eh stability fields for authigenic minerals (Fig. 3b), we estimated that the initial environments of formation for magnetite, millerite, siderite and vivianite correspond to the monimolimnion, SWI, shallow (<1–5 mblf) and deep sediments (>15 mblf), respectively. These precipitation stages, which are inherent to microbial processes, can overlap according to the geochemical gradient that develops in anoxic waters and sediments (Fig. 3a, b).

In Lake Towuti, some framboidal magnetites form as pelagic precipitates in the chemocline (Fig. 1c) during periods of water column stratification (Bauer *et al.*, 2020) and are preserved as such in the sediment (Fig. 2a). Even at low sulfate concentrations (<20 µM), microbial sulfate reduction in the vicinity of the SWI produces HS^- in pore water which preferentially reacts with Ni^{2+} over Fe^{2+} to form millerite, incorporating minor Fe and trace metals (Figs. 2b, S-2 and S-3). The spherical habits fused into acicular aggregates of authigenic millerites originating from microbial sulfate reduction appear in places with early siderite phases, or fully overgrown by siderite (Figs. 2b, S-3). Furthermore, millerite aggregates within siderite-rich zones (Fig. S-4) suggest increased millerite precipitation during deeper mixing phases and oxygenation of the sediment water interface, sulfate reduction taking place predominantly around the redox front within the upper few centimetres of the sediment column (Fig. S-5).

Crystallisation of successive phases from pore waters and the entangled habits that we observe (Fig. 2) reveal a certain degree of Ostwald ripening where smaller precursor crystals dissolve and re-precipitate allowing larger crystal nuclei to further grow over time of burial (Benning and Waychunas, 2008). As demonstrated for redox (trans)formation of green rust (Halevy *et al.*, 2017), pore water solutions become saturated with ferrous colloids (Moens *et al.*, 2021) that react with either carbonate or phosphate ions over time to form siderite monocrystals (Vuillemin *et al.*, 2019) and vivianite nodules (Vuillemin *et al.*, 2020). Siderite SEM images document diagenetic growth from micritic phases into twins and aggregates, forming spherules of mosaic monocrystals (Fig. 2c) promoted by saturated pore water conditions during burial (Table S-1). Similarly, vivianite SEM images reveal crystal growth from tabular habits into rosettes (Fig. 2d), forming macroscopic crystals due to diagenetic diffusion during burial, indicating that vivianite constitutes an important sink for Fe^{2+}, Mn^{2+} and Mg^{2+} in pore waters that reached saturation in specific sedimentary layers. Millerite and siderite inclusions identified in a vivianite crystal cross section suggest that these phases precipitated first (Fig. 2d). Finally, EDX results (Figs. 2, S-2) show that magnetites have minor trace metal concentrations, millerites incorporate some Fe^{2+}, siderites substitute Mn^{2+} in their initial growth phase, while later forming vivianites have an overall manganoan composition substituting both Mn^{2+} and Mg^{2+} (Kubeneck *et al.*, 2023).

Mineral biosignatures in their recent and ancient stratigraphic context. The mineralogy of Lake Towuti presents an alternation of dark green to reddish-grey clays, considered to reflect detrital iron fluxes to the lake, stratification regimes, and redox conditions at the SWI (Russell *et al.*, 2016, 2020). Variations in the burial of ferric iron and OM, their availability as substrates and the pore water geochemistry (Fig. 4) ensuing microbial breakdown, can imprint different mineral biosignatures during early diagenesis (Morlock *et al.*, 2021). Each of these minerals, whether forming in the water column, near surface sediments or from pore waters, acts as a discrete sink for selective solutes (*i.e.* Ni^{2+}, Mn^{2+}, Fe^{2+}, CO_3^{2-}, HS^-, PO_4^{3-}). Pore water profiles thereby provide constraints on the depth of formation and age difference with the stratigraphy. Yet their abundance along the stratigraphic record results from past depositional modes and redox biogeochemistry.

Iron inflows deposited under oxygenated conditions formed reddish clays containing abundant, but poorly reactive, detrital magnetites and diagenetic siderites (Vuillemin *et al.*, 2023). Millerites were also found in red clays in which slightly more sulfate was available for microbial reduction at the time of deposition (*i.e.* ~20 µM). These magnetites and millerites were progressively overgrown by diagenetic siderite during burial. While framboidal magnetites and spherical millerites represented pelagic precipitates forming under stratified conditions, vivianites nucleated from diffusive pore waters in greenish clays. To conclude, we could show that millerite precipitates in ferruginous anoxic waters and shallow sediments at sulfate levels relevant to sulfur cycling in Earth's early oceans (Farquhar *et al.*, 2010). Whereas vivianite preservation over a geologic scale is compromised, continuous precipitation of siderite from saturated pore waters forms spheroids that can coalesce into lithified bands like those documented in ancient red beds.

Acknowledgements

The financial, logistic and administrative support of the International Continental Scientific Drilling Program (ICDP), U.S. National Science Foundation (NSF), German Research Foundation (DFG), Swiss National Science Foundation (SNSF), PT Vale Indonesia, Ministry of Research, Education, and Higher Technology of Indonesia (RISTEK), U.S. National Lacustrine Core Repository, DOSECC Exploration Services, and GFZ German Research Centre for Geosciences is acknowledged. This study was financed through DFG grants of the ICDP priority program to JK (KA 2293/8-1) and AV (VU 94/1-1, VU 94/3-1), SNSF grants to AV (P2GEP2_148621) and HV (20FI21_153054/1, 200021_153053/1). AP and LGB acknowledge financial support from the Helmholtz Recruiting Initiative (I-044-16-01) for access to the Potsdam Imaging and Spectral Analyses (PISA) facility.

Editor: Andreas Kappler

Additional Information

Supplementary Information accompanies this letter at https://www.geochemicalperspectivesletters.org/article2339.

© 2023 The Authors. This work is distributed under the Creative Commons Attribution 4.0 License, which permits unrestricted use, distribution, and reproduction in any medium, provided the original author and source are credited. Additional information is available at http://www.geochemicalperspectivesletters.org/copyright-and-permissions.

Cite this letter as: Vuillemin, A., Morlock, M., Paskin, A., Benning, L.G., Henny, C., Kallmeyer, J., Russell, J.M., Vogel, H. (2023) Authigenic minerals reflect microbial control on pore waters in a ferruginous analogue. *Geochem. Persp. Let.* 28, 20–26. https://doi.org/10.7185/geochemlet.2339

References

Bauer, K.W., Byrne, J.M., Kenward, P., Simister, R.L., Michiels, C.C., Friese, A., Vuillemin, A., Henny, C., Nomosatryo, S., Kallmeyer, J., Kappler, A., Smit, M.A., Francois, R., Crowe, S.A. (2020) Magnetite biomineralization in ferruginous waters and early Earth evolution. *Earth and Planetary Science Letters* 549, 116495. https://doi.org/10.1016/j.epsl.2020.116495

Benning, L.G., Waychunas, G.A. (2008) Nucleation, Growth, and Aggregation of Mineral Phases: Mechanisms and Kinetic Controls. In: Brantley, S., Kubicki, J., White, A. (Eds.) *Kinetics of Water-Rock Interaction*. Springer, New York, 259–333. https://doi.org/10.1007/978-0-387-73563-4_7

Canfield, D.E., Poulton, S.W., Knoll, A.H., Narbonne, G.M., Ross, G., Goldberg, T., Strauss, H. (2008) Ferruginous Conditions Dominated Later Neoproterozoic Deep-Water Chemistry. *Science* 321, 949–952. https://doi.org/10.1126/science.1154499

Craw, D., Bowell, R.J. (2014) The Characterization of Arsenic in Mine Waste. *Reviews in Mineralogy and Geochemistry* 79, 473–505. https://doi.org/10.2138/rmg.2014.79.10

Fakhraee, M., Hancisse, O., Canfield, D.E., Crowe, S.A., Katsev, S. (2019) Proterozoic seawater sulfate scarcity and the evolution of ocean–atmosphere chemistry. *Nature Geoscience* 12, 375–380. https://doi.org/10.1038/s41561-019-0351-5

Farquhar, J., Wu, N., Canfield, D.E., Oduro, H. (2010) Connections between Sulfur Cycle Evolution, Sulfur Isotopes, Sediments, and Base Metal Sulfide Deposits. *Economic Geology* 105, 509–533. https://doi.org/10.2113/gsecongeo.105.3.509

Friese, A., Kallmeyer, J., Kitte, J.A., Montaño Martínez, I., Bijaksana, S., Wagner, D., the ICDP Lake Chalco Drilling Science Team, the ICDP Towuti Drilling Science Team (2017) A simple and inexpensive technique for assessing contamination during drilling operations. *Limnology and Oceanography: Methods* 15, 200–211. https://doi.org/10.1002/lom3.10159

Friese, A., Bauer, K., Glombitza, C., Ordoñez, L., Ariztegui, D., Heuer, V.B., Vuillemin, A., Henny, C., Nomosatryo, S., Simister, R., Wagner, D., Bijaksana, S., Vogel, H., Melles, M., Russell, J.M., Crowe, S.A., Kallmeyer, J. (2021) Organic matter mineralization in modern and ancient ferruginous sediments. *Nature Communications* 12, 2216. https://doi.org/10.1038/s41467-021-22453-0

Halevy, I., Alesker, M., Schuster, E.M., Popovitz-Biro, R., Feldman, Y. (2017) A key role for green rust in the Precambrian oceans and the genesis of iron formations. *Nature Geoscience* 10, 135–139. https://doi.org/10.1038/ngeo2878

Jiang, C.Z., Tosca, N.J. (2019) Fe(II)-carbonate precipitation kinetics and the chemistry of anoxic ferruginous seawater. *Earth and Planetary Science Letters* 506, 231–242. https://doi.org/10.1016/j.epsl.2018.11.010

Kubeneck, L.J., ThomasArrigo, L.K., Rothwell, K.A., Kaegi, R., Kretzschmar, R. (2023) Competitive incorporation of Mn and Mg in vivianite at varying salinity and effects on crystal structure and morphology. *Geochimica et Cosmochimica Acta* 346, 231–244. https://doi.org/10.1016/j.gca.2023.01.029

Maher, B.A., Alekseev, A., Alekseeva, T. (2003) Magnetic mineralogy of soils across the Russian Steppe: climatic dependence of pedogenic magnetite formation. *Palaeogeography, Palaeoclimatology, Palaeoecology* 201, 321–341. https://doi.org/10.1016/S0031-0182(03)00618-7

Mansor, M., Winkler, C., Hochella Jr., M.F., Xu, J. (2019) Nanoparticulate Nickel-Hosting Phases in Sulfidic Environments: Effects of Ferrous Iron and Bacterial Presence on Mineral Formation Mechanism and Solid-Phase Nickel Distribution. *Frontiers in Earth Science* 7, 151. https://doi.org/10.3389/feart.2019.00151

Moens, C., Montalvo, D., Smolders, E. (2021) The concentration and size distribution of iron-rich colloids in pore waters are related to soil organic matter content and pore water calcium concentration. *European Journal of Soil Science* 72, 2199–2214. https://doi.org/10.1111/ejss.13104

Morlock, M.A., Vogel, H., Nigg, V., Ordoñez, L.G., Hasberg, A.K.M., Melles, M., Russell, J.M., Bijaksana, S., the TDP Science Team (2018) Climatic and tectonic controls on source-to-sink processes in the tropical, ultramafic catchment of Lake Towuti, Indonesia. *Journal of Paleolimnology* 61, 279–295. https://doi.org/10.1007/s10933-018-0059-3

Morlock, M.A., Vogel, H., Russell, J.M., Anselmetti, F.S., Bijaksana, S. (2021) Quaternary environmental changes in tropical Lake Towuti, Indonesia, inferred from end-member modelling of X-ray fluorescence core-scanning data. *Journal of Quaternary Science* 36, 1040–1051. https://doi.org/10.1002/jqs.3338

Morton, S.C., Edwards, M. (2005) Reduced Phosphorus Compounds in the Environment. *Critical Reviews in Environmental Science and Technology* 35, 333–364. https://doi.org/10.1080/10643380590944978

Posth, N.R., Canfield, D.E., Kappler, A. (2014) Biogenic Fe(III) minerals: From formation to diagenesis and preservation in the rock record. *Earth-Science Reviews* 135, 103–121. https://doi.org/10.1016/j.earscirev.2014.03.012

Roh, Y., Zhang, C.-L., Vali, H., Lauf, R.J., Zhou, J., Phelps, T.J. (2003) Biogeochemical and environmental factors in Fe biomineralization: magnetite and siderite formation. *Clays and Clay Minerals* 51, 83–95. https://doi.org/10.1346/CCMN.2003.510110

Russell, J.M., Bijaksana, S., Vogel, H., Melles, M., Kallmeyer, J., Ariztegui, D., Crowe, S.A., Fajar, S., Hafidz, A., Haffner, D., Hasberg, A., Ivory, S., Kelly, C., King, J., Kirana, K., Morlock, M., Noren, A., O'Grady, R., Ordonez, L., Stevenson, J., von Rintelen, T., Vuillemin, A., Watkinson, I., Wattrus, N., Wicaksono, S., Wonik, T., Bauer, K., Deino, A., Friese, A., Henny, C., Imran, Marwoto, R., Ngkoimani, L.O., Nomosatryo, S., Safiuddin, L.O., Simister, R., Tamuntuan, G. (2016) The Towuti Drilling Project: paleoenvironments, biological evolution, and geomicrobiology of a tropical Pacific lake. *Scientific Drilling* 21, 29–40. https://doi.org/10.5194/sd-21-29-2016

Russell, J.M., Vogel, H., Bijaksana, S., Melles, M., Deino, A., Hafidz, A., Haffner, D., Hasberg, A.K.M., Morlock, M., von Rintelen, T., Sheppard, R., Stelbrink, B., Stevenson, J. (2020) The late quaternary tectonic, biogeochemical, and environmental evolution of ferruginous Lake Towuti, Indonesia. *Palaeogeography, Palaeoclimatology, Palaeoecology* 556, 109905. https://doi.org/10.1016/j.palaeo.2020.109905

Sheppard, R.Y., Milliken, R.E., Russell, J.M., Dyar, M.D., Sklute, E.C., Vogel, H., Melles, M., Bijaksana, S., Morlock, M.A., Hasberg, A.K.M. (2019) Characterization of iron in Lake Towuti sediment. *Chemical Geology* 512, 11–30. https://doi.org/10.1016/j.chemgeo.2019.02.029

Swanner, E.D., Lambrecht, N., Wittkop, C., Harding, C., Katsev, S., Torgeson, J., Poulton, S.W. (2020) The biogeochemistry of ferruginous lakes and past ferruginous oceans. *Earth-Science Reviews* 211, 103430. https://doi.org/10.1016/j.earscirev.2020.103430

Tosca, N.J., Jiang, C.Z., Rasmussen, B., Muhling, J. (2019) Products of the iron cycle on the early Earth. *Free Radical Biology and Medicine* 140, 138–153. https://doi.org/10.1016/j.freeradbiomed.2019.05.005

Vuillemin, A., Friese, A., Alawi, M., Henny, C., Nomosatryo, S., Wagner, D., Crowe, S.A., Kallmeyer, J. (2016) Geomicrobiological Features of Ferruginous Sediments from Lake Towuti, Indonesia. *Frontiers in Microbiology* 7, 1007. https://doi.org/10.3389/fmicb.2016.01007

Vuillemin, A., Horn, F., Friese, A., Winkel, M., Alawi, M., Wagner, D., Henny, C., Orsi, W.D., Crowe, S.A., Kallmeyer, J. (2018) Metabolical potential of microbial communities from ferruginous sediments. *Environmental Microbiology* 20, 4297–4313. https://doi.org/10.1111/1462-2920.14343

Vuillemin, A., Wirth, R., Kemnitz, H., Schleicher, A.M., Friese, A., Bauer, K.W., Simister, R., Nomosatryo, S., Ordoñez, L., Ariztegui, D., Henny, C., Crowe, S.A., Benning, L.G., Kallmeyer, J., Russell, J.M., Bijaksana, S., Vogel, H., the Towuti Drilling Project Science Team (2019) Formation of diagenetic siderite in modern ferruginous sediments. *Geology* 47, 540–544. https://doi.org/10.1130/G46100.1

Vuillemin, A., Friese, A., Wirth, R., Schuessler, J.A., Schleicher, A.M., Kemnitz, H., Lücke, A., Bauer, K.W., Nomosatryo, S., von Blanckenburg, F., Simister, R., Ordoñez, L.G., Ariztegui, D., Henny, C., Russell, J.M., Bijaksana, S., Vogel, H., Crowe, S.A., Kallmeyer, J., the Towuti Drilling Project Science Team (2020) Vivianite formation in ferruginous sediments from Lake Towuti, Indonesia. *Biogeosciences* 17, 1955–1973. https://doi.org/10.5194/bg-17-1955-2020

Vuillemin, A., Mayr, C., Schuessler, J.A., Friese, A., Bauer, K.W., Lücke, A., Heuer, V.B., Glombitza, C., Henny, C., von Blanckenburg, F., Russell, J.M., Bijaksana, S., Vogel, H., Crowe, S.A., Kallmeyer, J. (2023) A one-million-year isotope record from siderites formed in modern ferruginous sediments. *GSA Bulletin* 135, 504–522. https://doi.org/10.1130/B36211.1

Zachara, J.M., Kukkapadu, R.V., Fredrickson, J.K., Gorby, Y.A., Smith, S.C. (2002) Biomineralization of Poorly Crystalline Fe(III) Oxides by Dissimilatory Metal Reducing Bacteria (DMRB). *Geomicrobiology Journal* 19, 179–207. https://doi.org/10.1080/01490450252864271

Geochemical Perspectives Letters

© 2023 The Authors
Published by the European Association of Geochemistry

Authigenic minerals reflect microbial control on pore waters in a ferruginous analogue

A. Vuillemin, M. Morlock, A. Paskin, L.G. Benning, C. Henny, J. Kallmeyer, J.M. Russell, H. Vogel

Supplementary Information

The Supplementary Information includes:

- Supplementary Methods
- Figures S-1 to S-8
- Table S-1
- Supplementary Information References

Supplementary Methods

Core recovery, water column profiles, gravity cores

The oxygen concentration profile was collected on site using a submersible conductivity-temperature-depth probe (Sea-Bird SBE-19, Sea-Bird Electronics). The Fe^{2+} concentration profile was obtained from water samples (Bauer *et al*., 2020) collected using 5 L Niskin bottles (General Oceanics) attached in series and placed at depth using a commercial FCV 585 fish finder (Furuno Electric Co.). The upper 0.35 m of the sediment record corresponds to samples obtained *via* short gravity coring during pilot campaigns in November 2013 and 2014, and sampled as described in Vuillemin *et al*. (2016), whereas the 100-m-long sediment sequence comes from hydraulic cores obtained as part of the Towuti Drilling Project (TDP).

The TDP coring operations were carried out from May to July 2015 using the International Continental Scientific Drilling Program (ICDP) Deep Lakes Drilling System (Russell *et al*., 2016). Hole TDP-1A (156 m water depth) was drilled in May 2015 with a fluid contamination tracer added to the drill mud prior to operations and used to aid geomicrobiological sampling and analysis. All core sections were checked for contamination and those containing the tracer were discarded (Friese *et al*., 2017). Samples were collected from TDP-1A cores immediately upon recovery and were subsequently cut from the core sections into 5 and 10 cm long whole round cores (WRC), 6.6 cm in diameter, immediately capped and transferred to an anaerobic chamber flushed with nitrogen to avoid oxidation during sample handling, and processed in the field for analyses of pore water chemistry, cell count and microbial DNA fingerprinting.

In January 2016, the unsampled remainders of TDP-1A cores were split and scanned at the Limnological Research Center, Lacustrine Core Facility (LacCore), University of Minnesota, described macroscopically and microscopically to determine their stratigraphy and composition (Russell *et al*., 2016), then subsampled for dense mineral extraction (Vuillemin *et al*., 2019a).

Bulk analyses

Total organic carbon (TOC) was determined as the difference between elemental analyser (Total Carbon) and coulometric (Total Inorganic Carbon) analyses (Russell *et al*., 2020). Coulometric measurements were carried out at 60 °C with H_2SO_4 and a reaction time of 20 min. Siderite concentrations in bulk sediments were calculated based on mineral carbon values (MinC %) obtained from previous Rock-Eval analyses and corrected according to published equations of linear regression (Ordoñez *et al*., 2019). Results for siderite concentrations based on coulometric and Rock-Eval analyses were consistent, with about 20 % siderite in red clays at depth in the sediment succession.

For iron speciation, a subsample of 500 mg of wet sediment from each core interval of both sediment cores was extracted in the field and immediately leached in 1 mL 0.5 N HCl, and Fe-speciation (Fe^{II} and Fe^{III}) of the easily extractable Fe-phases was measured spectrophotometrically on site using a ferrozine assay (Viollier *et al*., 2000). For reactive and total Fe sequential extraction, the complete Fe-speciation protocol was performed on anoxically preserved and freeze-dried sediments milled to fine powders using an agate hand mortar and pestle. Sample masses of 200 mg of sediment were processed following the protocol described in (Poulton and Canfield, 2005). The highly reactive Fe pool is defined as the sum of hydrous Fe (oxyhydr)oxides including ferrihydrite and lepidocrocite (0.5 N HCl extractable Fe), carbonate-associated Fe (acetate extractable Fe), ferric (oxyhydr)oxides including hematite and goethite (dithionite extractable Fe), and magnetite ($Fe^{2+}Fe_2^{3+}O_4$) (oxalate extractable Fe). These reagents do not extract the Fe present in pyrite ($Fe^{2+}S_2$) (Henkel *et al*., 2018). The non-reactive Fe pool is defined as Fe contained in silicate minerals after removal of reactive phases (near boiling 6 N HCl extractable Fe). Total Fe was obtained by summing up the highly reactive Fe pools and the non-reactive Fe contained in silicate minerals (Fig. S-1). The entire procedure is detailed in (Friese *et al*., 2021).

Pore water sampling and geochemical analyses

Pore water within the upper 10 m of TDP-1A cores was extracted using Rhizon Pore Water Samplers (Rhizosphere research products), directly inserted into the soft sediment. Below 10 m depth, we removed the more compact sediment samples from their liner and scraped off all potentially contaminated rims with a sterile spatula. The remaining sediment was transferred into an IODP-style titanium pore water extraction cylinder and placed on a two-column bench top laboratory hydraulic press (Carver Inc.). Pore water was filtered through a sterile 0.2 µm syringe filter and collected in a glass syringe pre-flushed with nitrogen. For anion analysis, 1 mL of pore water was transferred to a screw neck glass vial (VWR International) and stored at 4 °C until analysis. Alkalinity, pH, and Fe^{2+} concentrations were determined in the field *via* colourimetric titration, potentiometry and spectrophotometry, respectively. Major ions were analysed at GFZ Potsdam by ion chromatography.

The pH was measured in the field with a portable pH metre (Thermo Scientific Orion, Star A321) calibrated at pH = 4, 7 and 10. We homogenised 2 mL of sediment in 2 mL of deionised water and measured the supernatant after 2 min and calibrated our results based on standard reference materials, as commonly done for organic-rich soil samples (Black, 1973). Total alkalinity was measured *via* colourimetric titration on pore water samples. Dissolved inorganic carbon (DIC) concentrations were calculated by solving the carbonate system using the pH and alkalinity profiles and borehole temperatures (Jenkins and Moore, 1977). Dissolved Fe^{2+} concentrations were measured directly after pore water retrieval using 1 mL aliquots transferred to 1.6 mL Rotilabo single-use cells (Carl Roth) and stabilised by adding 100 µL of Ferrozine Iron Reagent (Sigma-Aldrich Chemie). Absorbance of the coloured solution was measured at 562 nm with a DR 3900 spectrophotometre (Hach). To determine pore water total Fe concentrations, 150 µL of hydroxylamine hydrochloride were added to 800 µL of the previous mixture, left to react 10 min to reduce all dissolved Fe^{3+}, stabilised by adding 50 µL ammonium acetate and absorbance of the solution measured a second time (Viollier *et al*., 2000). Pore water total Fe concentrations were found to be the same as Fe^{2+} concentrations, and thus Fe^{3+} is absent in pore water. Detection limit of the method is 0.25 µM. Concentrations of Mn^{2+} were analysed *via* spectrophotometry

as previously published (Jones *et al*., 2011), following the formaldoxime method (Brewer and Spencer, 1971). Concentrations of PO_4^{3-} in pore water were measured in the field by spectrophotometry. We aliquoted 0.5 mL pore water to 1.5 mL disposable cuvettes (Brand Gmbh) and added 80 µL colour reagent consisting of ammonium molybdate containing ascorbic acid and antimony. Absorbance was measured at 882 nm with a DR 3900 spectrophotometre (Hach). Detection limit of the method is 0.05 µM. Pore water Ca^{2+}, Mg^{2+}, SO_4^{2-} and NH_4^+ concentrations were analysed by normal and suppressed ion chromatography. Based on signal-to-noise ratios of 3 and 10, respective detection and quantification limits of the method calibrated on a multi-element standard are 8.3 and 38.5 µM for Ca^{2+}, 9.6 and 44.6 µM for Mg^{2+}, 2.0 and 8.4 µM for SO_4^{2-}, and 11.3 and 67.6 µM for NH_4^+. All samples were measured in triplicates, with reproducibility better than 5 %. All procedures were previously published (Vuillemin *et al*., 2016, 2023).

The concentrations of trace metals in pore water (*i.e.* As, Co) were measured *via* inductively coupled plasma mass spectrometry (ICP-MS). For this purpose, 100 µL of pore water sample were added to 10 mL of HNO_3 2 % with 10 µL of standard solution, mixed thoroughly, and then measured using a ThermoFischer HR-ICP-MS system. Concentrations of trace elements in pore water were calculated based on the standard spiked in the sample.

Concentrations of formate, lactate, acetate, butyrate and propionate in the pore water were measured by 2-dimensional ion chromatography mass spectrometry (2D IC-MS) (Glombitza *et al*., 2014). Measurements were performed with a Dionex ICS3000 ion chromatograph coupled to a Surveyor MSQ Plus mass spectrometre (both Thermo Scientific). The first chromatograph dimension separates the volatile fatty acids (VFAs) from other inorganic ions by trapping them on a concentrator column and subsequently separating them in the second chromatography dimension. Prior to analysis, pore water samples were filtered through disposable syringe filters (Acrodisc 13 mm IC, pore size 0.2 µm) rinsed with 10 mL ultrapure Milli-Q water directly before use. The first 0.5 mL of filtered pore water was discarded and the second 0.5 mL used for analysis. Quantification was achieved by a three-point calibration with external standards containing a mixture of the analysed VFAs at different concentrations (*i.e.* 200, 500 and 800 µg L^{-1}). Detection limits for formate and acetate were 0.37 and 0.19 µM, respectively. For methane analysis, 2 cm^3 of sediment were transferred on site inside the anaerobic chamber with a cut-off syringe to a 20 mL crimp vial filled with saturated NaCl solution and stored at 4 °C. For analysis, 3 mL helium (He) was introduced to form a headspace followed by 12 h equilibration. Methane concentration was determined by injecting 200 µL of the He headspace into a Thermo Finnigan Trace gas chromatograph (Thermo Fisher Scientific) equipped with a flame ionisation detector (Heuer *et al*., 2009).

Potential sulfate reduction rates (pSRRs) were determined by sediment incubation (Kallmeyer *et al*., 2004) with radioactive $^{35}SO_4^{2-}$ using sterile glass plug mini-cores processed in triplicates (Friese *et al*., 2021). The microbially reduced inorganic sulfur species were separated using a cold chromium distillation (Kallmeyer *et al*., 2004) and radioactivity in the extracts quantified using Ultima Gold Scintillation Cocktail (Perkin Elmer, Waltham) and a Tri-Carb 2500 TR liquid scintillation counter (Packard Instruments).

XRF core-scanning elemental profiles on bulk sediment

All cores used in the splice composite sequence covering the upper 100 m of sediments recovered from TDP Site 1 (106 split-core sections) were scanned on a XRF core scanner (ITRAX, Cox Ltd., Sweden) equipped with a chromium anode X-ray tube (Cr-tube) set to 30 kV, 50 mA and 50 s integration time at 5 mm resolution. Measurements were repeated with a molybdenum anode X-ray tube (Mo-tube) with the same settings to resolve elements with high atomic numbers (Morlock *et al*., 2021).

Sporadic event layers (tephra and turbidites) as well as intervals with low XRF performance and gaps related to uneven core surfaces were removed from the dataset during post-processing. The dataset was mathematically corrected *via* a multivariate log-ratio calibration (MCL) algorithm and data transformation (Weltje and Tjallingi, 2008) on the ItraXelerate software v. 2.4 (Bloemsma *et al.*, 2012). This correction allows for the estimation of values in weight % [wt. %] for all elements measured through XRF.

Mineral extraction and SEM imaging

In the field, core catchers were packed into gas-tight aluminum foil bags flushed with nitrogen gas and heat-sealed to keep them under anoxic conditions until mineral extraction. Minerals from core catcher sediments were extracted after 3 months of storage, whereas siderite and vivianite crystals from split TDP-1A cores were extracted from sediment beds with macroscopic enrichment in these phases after 8 months of storage at LacCore. Siderite, millerite and vivianite crystals were retrieved *via* density separation and sorted by placing a neodymium magnet under the beaker and rinsing out the non-magnetic fraction with deionised water (Vuillemin *et al*., 2019a).

Morphological investigation and elemental analysis of the dense mineral fractions obtained from a volume of 50 mL of sediment were processed *via* scanning electron microscopy (SEM) coupled to energy dispersive X-ray spectroscopy (EDX). The samples were prepared by putting an extract of dense minerals or macroscopic crystals onto carbon coated disc which was glued onto SEM aluminum stubs. The samples were carbon coated (~20 nm layer) using a Leica EM ACE600 high-vacuum sputter coater. SEM analysis was performed on a Zeiss Ultra 55 Plus field SEM (for siderites) and on a FEI Quanta 3D FEG (for millerites) at a voltage of 20 kV acceleration voltage. Elemental composition of the imaged samples was determined based on SEM-EDX point and area analyses *via* Octane Elect detector from EDAX (Ametek Inc.). EDX data analysis and acquisition was performed on the EDAX-APEX EDX interface software (Ametek Inc.).

Data accessibility

The present scientific data are archived and publicly available from the PANGAEA® Data Publisher for Earth and Environmental Science (datasets #908080 and #934401) (Vuillemin *et al*., 2019b, 2021).

Supplementary Figures

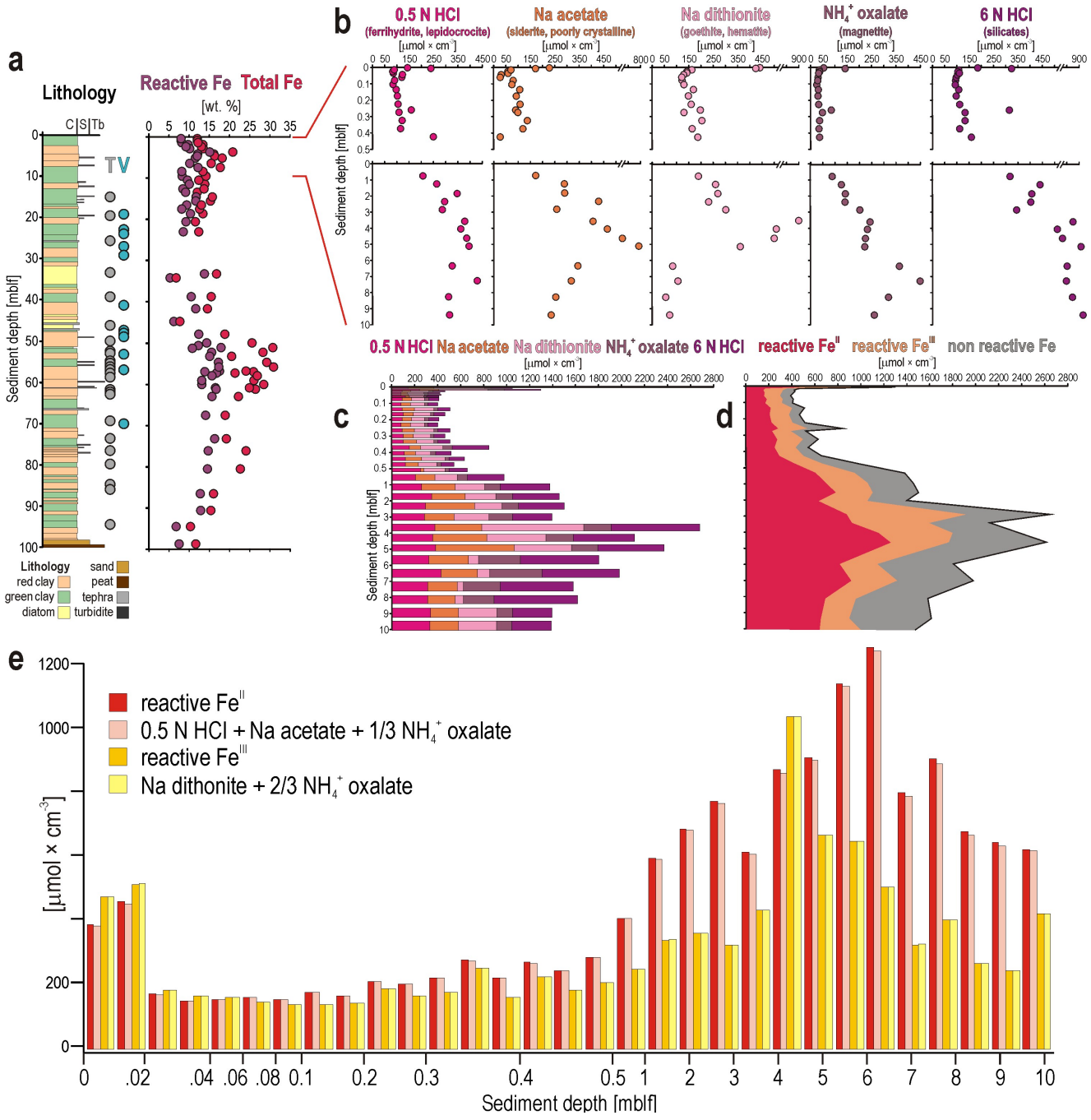

Figure S-1 Additional depth profiles for bulk iron and sequentially extracted iron phases. **(a)** Stratigraphy of site TDP-1A and reactive and total iron. **(b)** Separate and **(c)** cumulative plots for iron fractions sequentially extracted with solutions of 0.5 N HCl, sodium acetate adjusted to pH 4.5, sodium dithionite adjusted to pH 4.8, 0.2 M ammonium oxalate with 0.17 M oxalic acid adjusted to pH 3.2, and near boiling 6 N HCl. **(d)** Iron speciation was determined spectrophotometically. Note that Fe^{III} within the 0.5 N HCl fraction was below detection, so that the reactive Fe^{III} pool is entirely composed of the sodium dithionite (*e.g.*, goethite, hematite) and ammonium oxalate (*e.g.*, magnetite) fractions. **(e)** Close-up of the cumulative plot for sequentially extracted iron fractions (modified from Friese *et al.*, 2021).

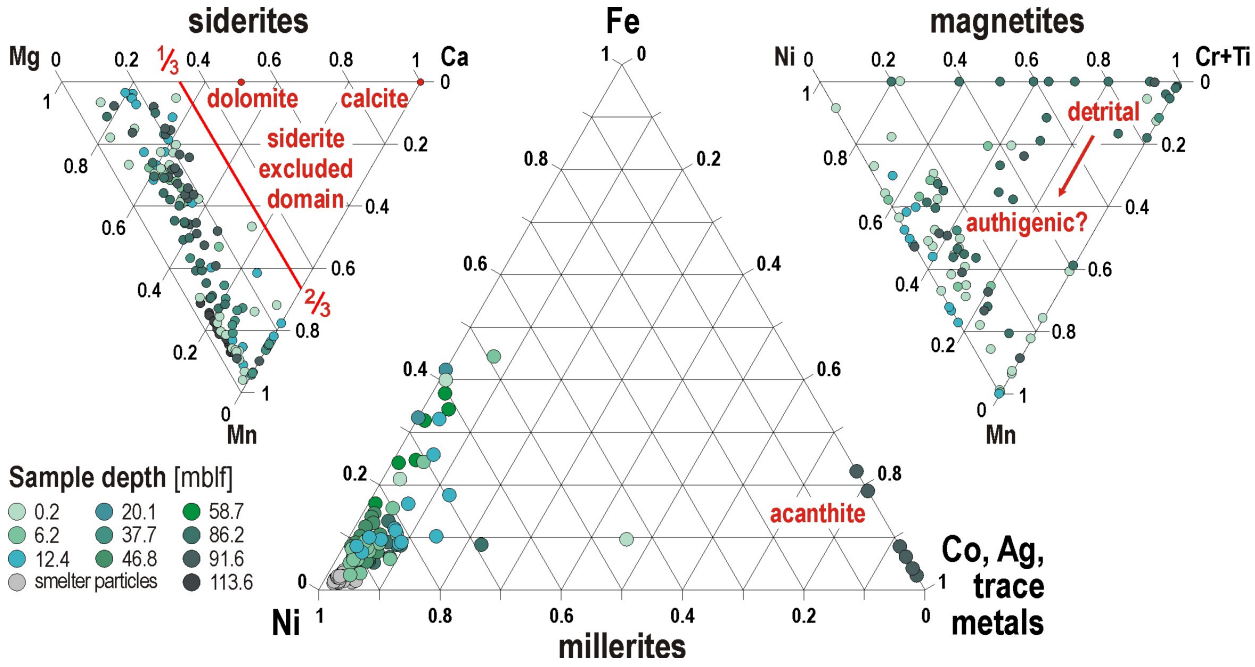

Figure S-2 Elemental EDX point analyses. The ternary plots show that millerites include minor Fe^{2+} traces **(centre)**. Acanthite (ac) was also identified in deep sediments (see Fig. S-8). Siderites **(left)** substitute Mn^{2+} for Fe^{2+} in the initial growth phase, incorporating variable amount of Mg^{2+} but constant Ca^{2+} traces in crystal rims. Magnetites **(right)** show some indication of trace metal incorporation related to microbial reduction. Although trace elements (*e.g.*, Ni, Mn, Ti and Cr) are common in magmatic magnetites, increased Mn and Ni contents potentially point to neoformation of magnetites in the water column (Bauer *et al.*, 2020) and sediment (Vuillemin *et al.*, 2019a).

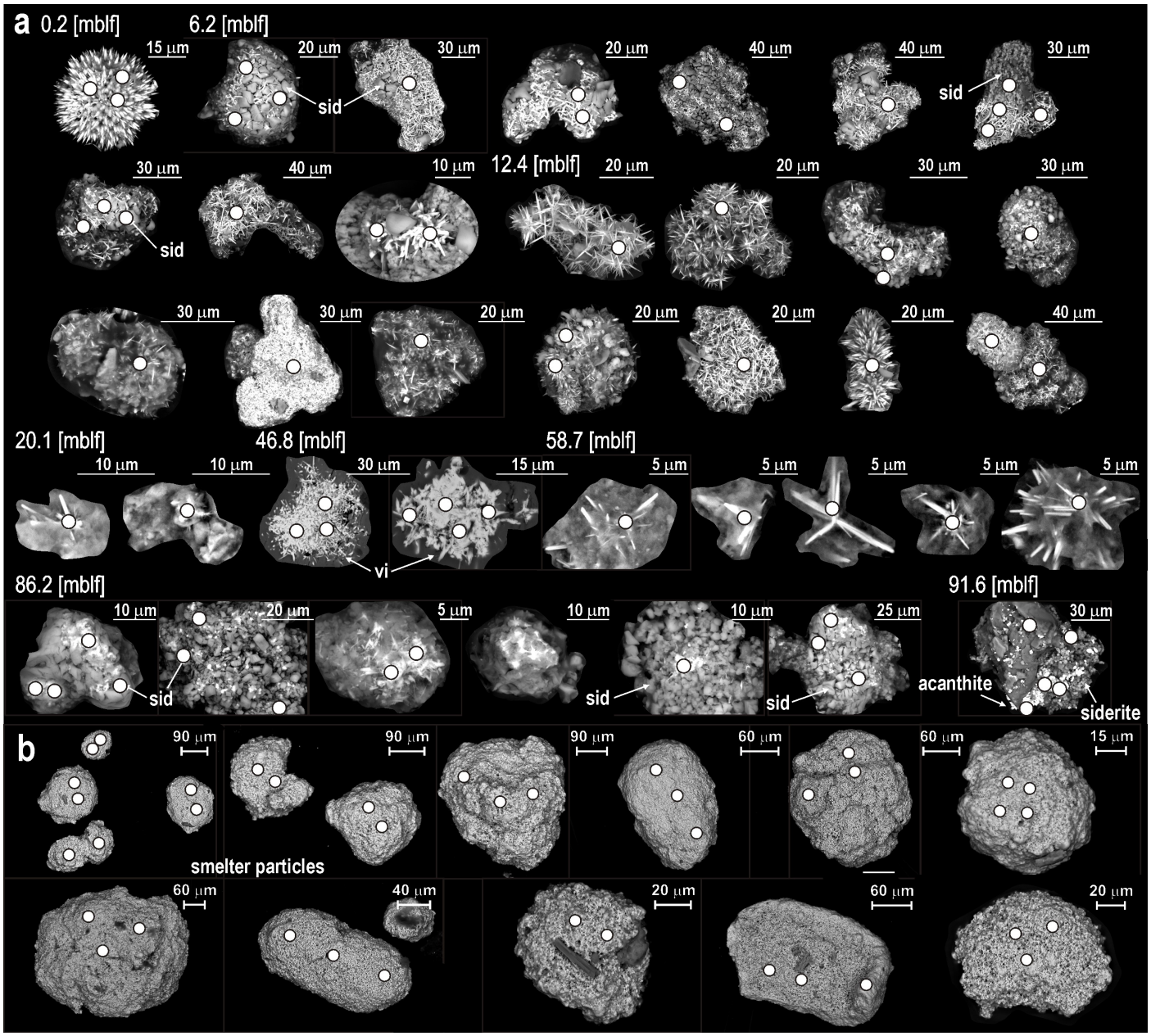

Figure S-3 SEM images of millerites and corresponding points of EDX analyses. **(a)** Millerite crystals identified in dense fractions, sometime entangled with siderite or as inclusions in vivianites, and corresponding points of EDX analyses. Acanthite was identified in a sample from 91.6 mblf (see Fig. S-8). **(b)** Millerite dust contaminants (*i.e.* smelter particles) derived from Sorowako's nickel mine smelter and corresponding points of EDX analyses.

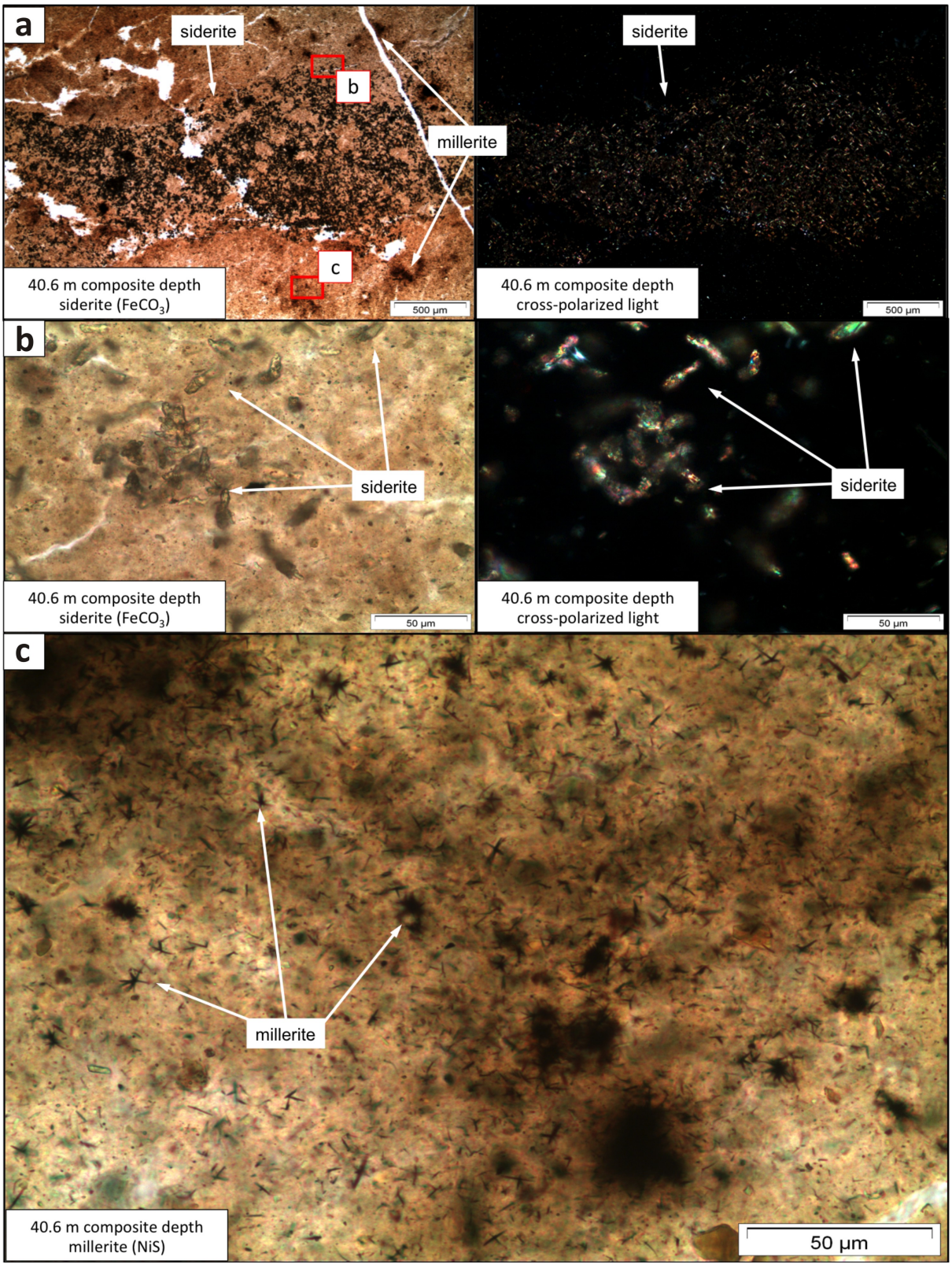

Figure S-4 Optical images of sediment smear slides in natural and polarised light. The density of siderite and millerite crystals in the vicinity of micro-cracks in the sediment argue for secondary precipitation from pore water associated with the additional pore space accommodated during seismic events with **(a–c)** close-ups to millerite crystals.

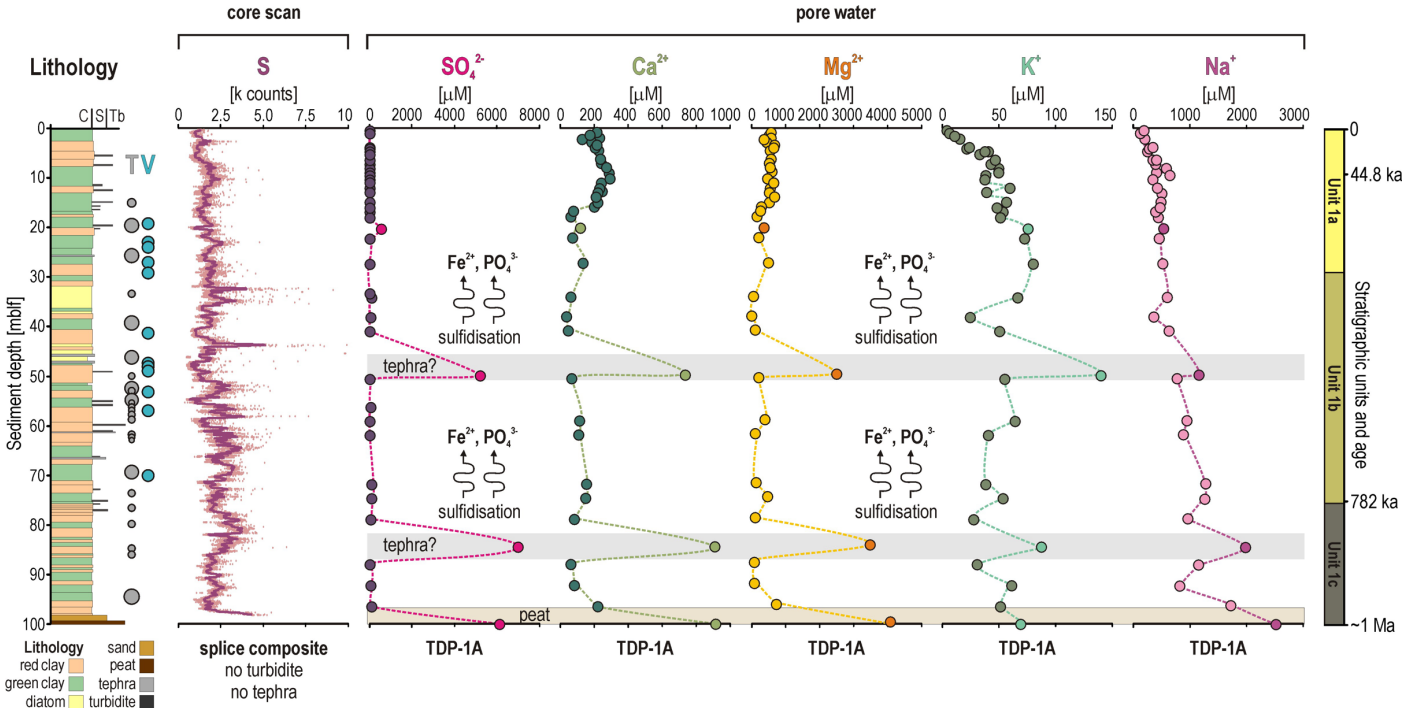

Figure S-5 Depth profiles for bulk sediment, and pore water geochemistry. **(Left to right)** Stratigraphy of site TDP-1A; XRF core-scanning profile for total S; pore water concentrations for SO_4^{2-}, Ca^{2+}, Mg^{2+}, K^+ and Na^+. The outliers in pore water concentrations may be explained by sporadic tephra and dissolution of anhydrite ($CaSO_4$) and sanidine ($KAlSi_3O_8$). An additional source of sulfate to the lake could result in sulfidisation of iron oxides (*e.g.*, goethite, hematite) with subsequent release and diffusion of pore water Fe^{2+} and PO_4^{3-} that would promote saturated conditions with respect to vivianite. Similarly, microbial acid-sulfate weathering of basaltic tephra could (trans)form ferric minerals, *e.g.*, jarosite [$(K, Na, H_3O)Fe^{3+}_3(SO_4)_2(OH)_6$], to release sulfate (Sekerci and Balci, 2022). Stratigraphic units correspond to: **(Unit 1c)** lake initial stage with basin subsidence and regular riverine-deltaic inflows; **(Unit 1b)** a productive phase with low sedimentation rates; and **(Unit 1a)** hydrological changes and lake level fluctuations during the Late Pleistocene (Russell *et al*., 2020; Vuillemin *et al*., 2023).

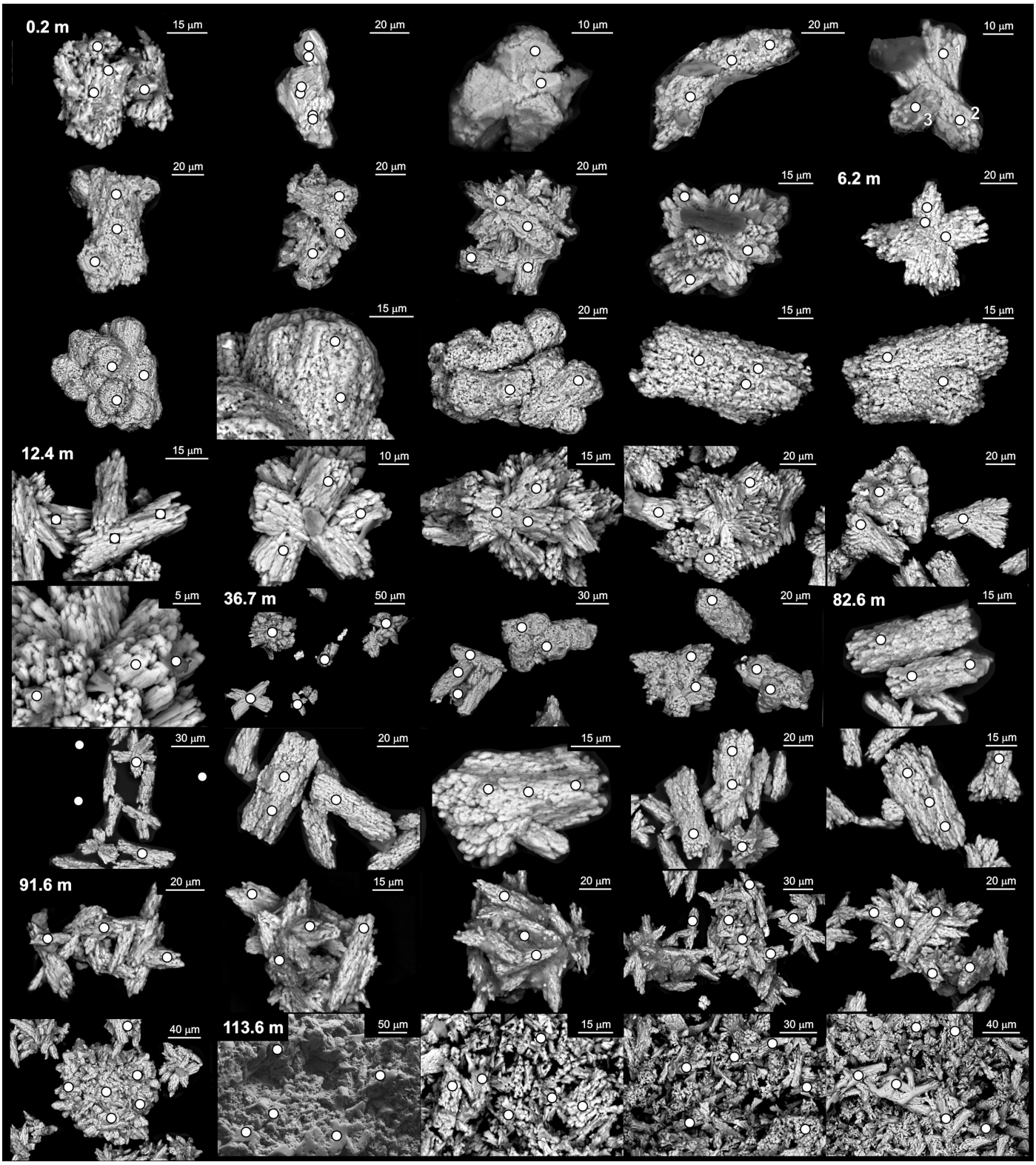

Figure S-6 SEM images of siderites and corresponding points of EDX analyses.

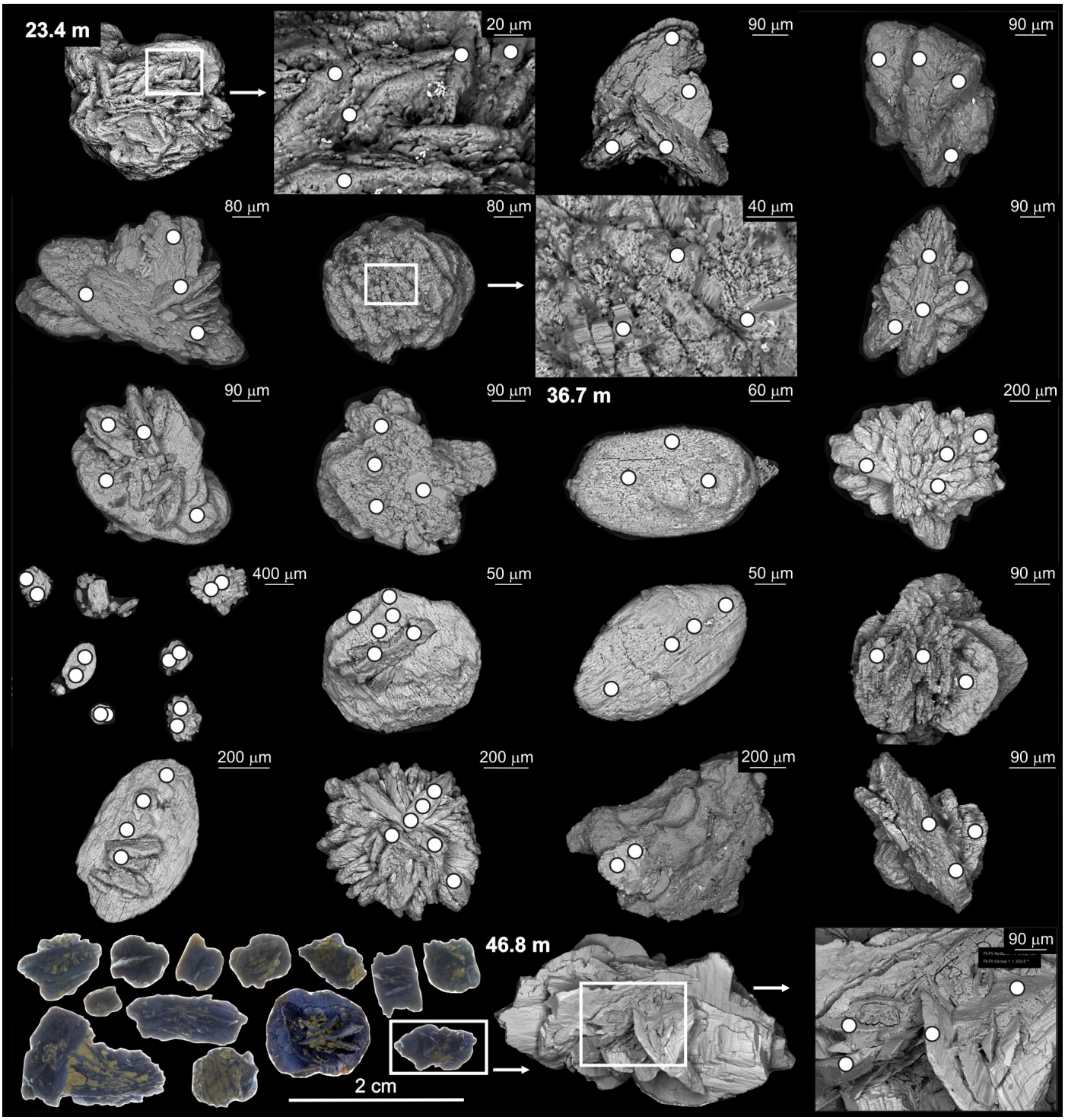

Figure S-7 SEM images of vivianites and corresponding points of EDX analyses.

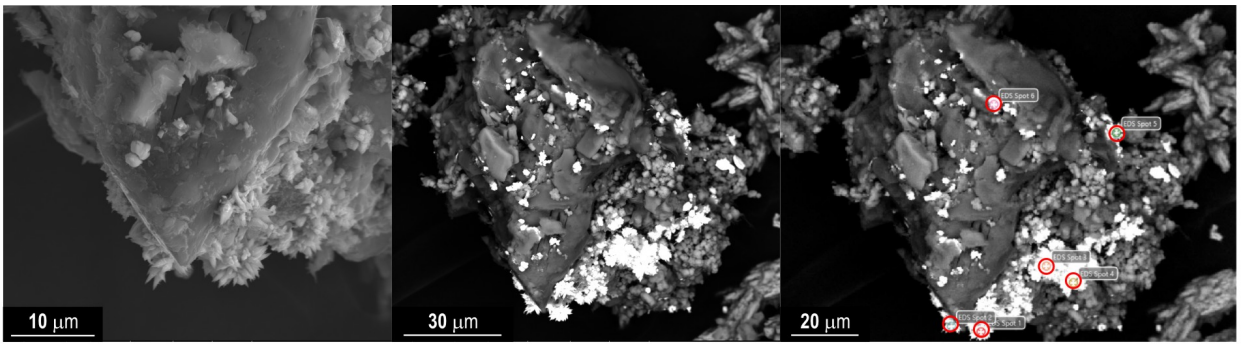

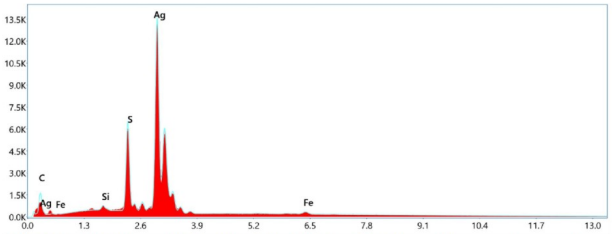

Element	Weight %	MDL	Atomic %	Net Int.	Error %	R	A	F
C K	13.6	0.58	52.0	470.1	12.4	0.7458	0.0897	1.0000
Si K	0.4	0.09	0.7	240.3	13.5	0.7972	0.4811	1.0202
S K	10.0	0.09	14.4	5722.3	4.9	0.8087	0.6786	1.0377
Fe K	1.1	0.29	0.9	214.5	17.9	0.8660	0.8709	1.0630
Ag L	74.9	0.29	32.0	13880.4	3.6	0.8233	0.7691	1.0038

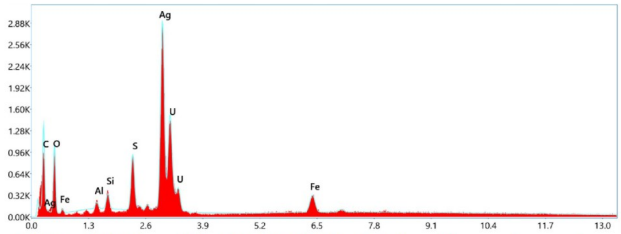

Element	Weight %	MDL	Atomic %	Net Int.	Error %	R	A	F
C K	33.2	0.64	59.1	695.9	11.1	0.8393	0.1274	1.0000
O K	22.0	0.55	29.5	606.9	12.3	0.8535	0.0652	1.0000
Al K	0.4	0.13	0.3	77.0	20.6	0.8806	0.4314	1.0088
Si K	0.7	0.12	0.5	184.9	11.1	0.8854	0.5504	1.0133
S K	3.0	0.10	2.0	771.7	5.6	0.8944	0.7379	1.0276
Fe K	4.1	0.37	1.6	365.3	7.9	0.9342	0.9311	1.0667
Ag L	34.0	0.31	6.7	2921.5	3.5	0.9054	0.8436	1.0047
U M	2.7	1.38	0.2	191.8	9.6	0.9081	0.8582	1.0176

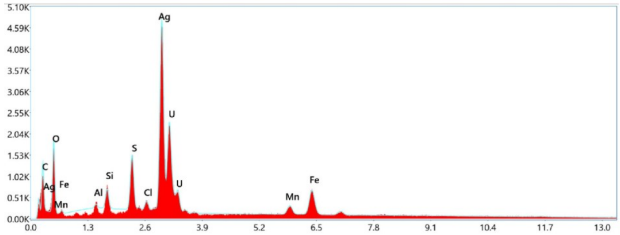

Element	Weight %	MDL	Atomic %	Net Int.	Error %	R	A	F
C K	23.3	0.72	47.2	635.1	11.7	0.8258	0.1114	1.0000
O K	24.1	0.55	36.7	1045.5	11.5	0.8403	0.0689	1.0000
Al K	0.3	0.13	0.2	78.4	23.3	0.8686	0.4056	1.0092
Si K	1.0	0.12	0.9	382.8	9.1	0.8736	0.5256	1.0140
S K	3.3	0.10	2.5	1235.8	5.8	0.8831	0.7176	1.0295
Cl K	0.1	0.14	0.1	41.4	61.8	0.8876	0.7669	1.0448
Mn K	2.0	0.29	0.9	285.2	12.3	0.9215	0.9071	1.0582
Fe K	6.4	0.36	2.8	834.0	5.3	0.9257	0.9255	1.0604
Ag L	38.2	0.31	8.6	4808.8	3.5	0.8947	0.8293	1.0049
U M	1.3	1.03	0.1	130.7	16.7	0.8977	0.8453	1.0219

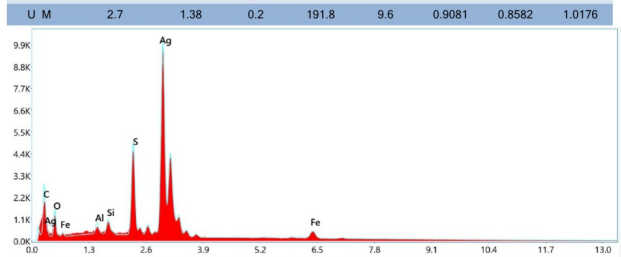

Element	Weight %	MDL	Atomic %	Net Int.	Error %	R	A	F
C K	28.7	0.52	60.2	1246.1	11.1	0.8152	0.1003	1.0000
O K	13.2	0.44	20.9	822.5	12.3	0.8299	0.0559	1.0000
Al K	0.8	0.08	0.8	447.7	10.9	0.8589	0.4212	1.0113
Si K	0.9	0.07	0.8	618.0	8.1	0.8641	0.5360	1.0174
S K	6.6	0.07	5.2	4471.7	4.5	0.8739	0.7240	1.0334
Fe K	2.2	0.20	1.0	513.0	9.4	0.9187	0.9142	1.0647
Ag L	47.5	0.21	11.1	10438.0	3.2	0.8860	0.8166	1.0039

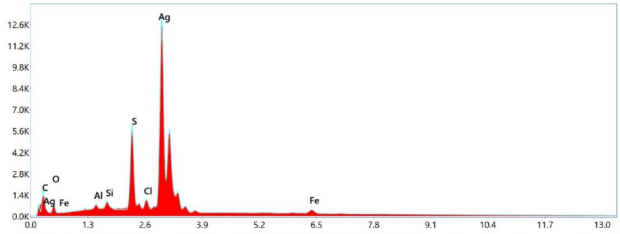

Element	Weight %	MDL	Atomic %	Net Int.	Error %	R	A	F
C K	17.0	0.58	50.5	657.2	12.0	0.7724	0.0915	1.0000
O K	7.3	0.49	16.2	395.7	13.2	0.7872	0.0502	1.0000
Al K	0.5	0.10	0.6	235.8	15.6	0.8181	0.3840	1.0122
Si K	0.7	0.08	0.9	420.4	10.4	0.8238	0.4986	1.0190
S K	8.3	0.08	9.2	5243.6	4.8	0.8348	0.6933	1.0365
Cl K	0.5	0.13	0.5	280.6	16.2	0.8401	0.7188	1.0552
Fe K	1.5	0.26	0.9	319.3	15.8	0.8876	0.8873	1.0635
Ag L	64.3	0.26	21.2	13268.3	3.5	0.8486	0.7854	1.0038

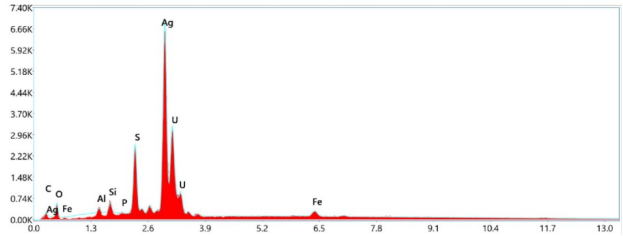

Element	Weight %	MDL	Atomic %	Net Int.	Error %	R	A	F
C K	4.4	0.77	18.1	87.7	17.4	0.7429	0.0947	1.0000
O K	10.5	0.66	32.4	295.5	13.5	0.7572	0.0521	1.0000
Al K	0.6	0.16	1.1	128.1	17.8	0.7884	0.3517	1.0109
Si K	1.0	0.14	1.8	287.4	11.5	0.7943	0.4631	1.0166
P K	0.0	0.10	0.1	8.9	73.8	0.8002	0.5652	1.0263
S K	7.6	0.13	11.7	2276.0	5.5	0.8059	0.6601	1.0322
Fe K	2.4	0.42	2.2	265.2	13.6	0.8636	0.8705	1.0640
Ag L	69.7	0.39	32.0	7036.8	3.8	0.8205	0.7683	1.0041
U M	3.8	1.60	0.8	318.8	11.6	0.8244	0.7848	1.0169

Figure S-8 SEM images of acanthite and corresponding points of EDX analyses.

Supplementary Table

Table S-1 Modelled saturation indices based on pH, alkalinity, pore water concentrations of major ions and borehole temperatures.

SUPPLEMENTARY TABLE S-1. MODELLED SATURATION INDICES

5 m: zone 1	Saturation	10 m: zone 2	Saturation	35 m: zone 4	Saturation
talc/serpentine	**1.43**	**siderite**	**1.00**	**siderite**	**1.00**
siderite	**1.29**	quartz	0.71	quartz	0.71
quartz	0.71	chalcedony	0.29	chalcedony	0.29
chalcedony	0.29	**vivianite**	**-0.04**	**vivianite**	**-0.04**
vivianite	**-0.45**	**talc/serpentine**	**-0.31**	**talc/serpentine**	**-0.31**
α SiO_2	-0.54	α SiO_2	-0.54	α SiO_2	-0.54
calcite	-0.68	calcite	-0.83	calcite	-0.83
dolomite	-0.77	aragonite	-0.97	aragonite	-0.97
aragonite	-0.82	dolomite	-1.27	dolomite	-1.27

Supplementary Information References

Bauer, K.W., Byrne, J.M., Kenward, P., Simister, R.L., Michiels, C.C., Friese, A., Vuillemin, A., Henny, C., Nomosatryo, S., Kallmeyer, J., Kappler, A., Smit, M.A., Francois, R., Crowe, S.A. (2020) Magnetite biomineralization in ferruginous waters and early Earth evolution. *Earth and Planetary Science Letters* 549, 116495. https://doi.org/10.1016/j.epsl.2020.116495

Black, C.A. (1973) Methods of soil analysis: test methods for evaluating solid waste. In: *Physical/Chemical Methods, 9045B Soil and Waste pH*. American Society of Agronomy, Madison, USA. https://www.epa.gov/hw-sw846/sw-846-test-method-9045d-soil-and-waste-ph

Bloemsma, M.R., Zabel, M., Stuut, J.B.W., Tjallingii, R., Collins, J.A., Weltje, G.J. (2012) Modelling the joint variability of grain size and chemical composition in sediments. *Sedimentary Geology* 280, 135–148. https://doi.org/10.1016/j.sedgeo.2012.04.009

Brewer, P.G., Spencer, D.W. (1971) Colorimetric determination of manganese in anoxic waters. *Limnology and Oceanography* 16, 107–110. https://doi.org/10.4319/lo.1971.16.1.0107

Friese, A., Kallmeyer, J., Kitte, J.A., Montaño Martínez, I., Bijaksana, S., Wagner, D., the ICDP Lake Chalco Drilling Science Team, the ICDP Towuti Drilling Science Team (2017) A simple and inexpensive technique for assessing contamination during drilling operations. *Limnology and Oceanography: Methods* 15, 200–211. https://doi.org/10.1002/lom3.10159

Friese, A., Bauer, K., Glombitza, C., Ordoñez, L., Ariztegui, D., Heuer, V.B., Vuillemin, A., Henny, C., Nomosatryo, S., Simister, R., Wagner, D., Bijaksana, S., Vogel, H., Melles, M., Russell, J.M., Crowe, S.A., Kallmeyer, J. (2021) Organic matter mineralization in modern and ancient ferruginous sediments. *Nature Communications* 12, 2216. https://doi.org/10.1038/s41467-021-22453-0

Henkel, S., Kasten, S., Hartmann, J.F., Silva-Busso, A., Staubwasser, M. (2018) Iron cycling and stable Fe isotope fractionation in Antarctic shelf sediments, King George Island. *Geochimica et Cosmochimica Acta* 237, 320–338. https://doi.org/10.1016/j.gca.2018.06.042

Heuer, V.B., Pohlman, J.W., Torres, M.E., Elvert, M., Hinrichs, K.-U. (2009) The stable carbon isotope biogeochemistry of acetate and other dissolved carbon species in deep subseafloor sediments at the northern Cascadia Margin. *Geochimica et Cosmochimica Acta* 73, 3323–3336. https://doi.org/10.1016/j.gca.2009.03.001

Glombitza, C., Pedersen, J., Røy, H., Jørgensen, B.B. (2014) Direct analysis of volatile fatty acids in marine sediment porewater by two-dimensional ion chromatography-mass spectrometry. *Limnology and Oceanography: Methods* 12, 455–468. https://doi.org/10.4319/lom.2014.12.455

Jenkins, S.R., Moore, R.C. (1977) A Proposed Modification to the Classical Method of Calculating Alkalinity in Natural Waters. *Journal AWWA* 69, 56–60. https://doi.org/10.1002/j.1551-8833.1977.tb02544.x

Jones, C., Crowe, S.A., Sturm, A., Leslie, K.L., MacLean, L.C.W., Katsev, S., Henny, C., Fowle, D.A., Canfield, D.E. (2011) Biogeochemistry of manganese in ferruginous Lake Matano, Indonesia. *Biogeosciences* 8, 2977–2991. https://doi.org/10.5194/bg-8-2977-2011

Kallmeyer, J., Ferdelman, T.G., Weber, A., Fossing, H., Jørgensen, B.B. (2004) A cold chromium distillation procedure for radiolabeled sulfide applied to sulfate reduction measurements. *Limnology and Oceanography: Methods* 2, 171–180. https://doi.org/10.4319/lom.2004.2.171

Morlock, M.A., Vogel, H., Russell, J.M., Anselmetti, F.S., Bijaksana, S. (2021) Quaternary environmental changes in tropical Lake Towuti, Indonesia, inferred from end-member modelling of X-ray fluorescence core-scanning data. *Journal of Quaternary Science* 36, 1040–1051. https://doi.org/10.1002/jqs.3338

Ordoñez, L., Vogel, H., Sebag, D., Ariztegui, D., Adatte, T., Russell, J.M., Kallmeyer, J., Vuillemin, A., Friese, A., Crowe, S.A., Bauer, K.W., Simister, R., Henny, C., Nomosatryo, S., Bijaksana, S., the Towuti Drilling Project Scientific Team (2019) Empowering conventional Rock-Eval pyrolysis for organic matter characterization of the siderite-rich sediments of Lake Towuti (Indonesia) using End-Member Analysis. *Organic Geochemistry* 134, 32–44. https://doi.org/10.1016/j.orggeochem.2019.05.002

Poulton, S.W., Canfield, D.E. (2005) Development of a sequential extraction procedure for iron: implications for iron partitioning in continentally derived particulates. *Chemical Geology* 214, 209–221. https://doi.org/10.1016/j.chemgeo.2004.09.003

Russell, J.M., Bijaksana, S., Vogel, H., Melles, M., Kallmeyer, J., Ariztegui, D., Crowe, S.A., Fajar, S., Hafidz, A., Haffner, D., Hasberg, A., Ivory, S., Kelly, C., King, J., Kirana, K., Morlock, M., Noren, A., O'Grady, R., Ordonez, L., Stevenson, J., von Rintelen, T., Vuillemin, A., Watkinson, I., Wattrus, N., Wicaksono, S., Wonik, T., Bauer, K., Deino, A., Friese, A., Henny, C., Imran, Marwoto, R., Ngkoimani, L.O., Nomosatryo, S., Safiuddin, L.O., Simister, R., Tamuntuan, G. (2016) The Towuti Drilling Project: paleoenvironments, biological evolution, and geomicrobiology of a tropical Pacific lake. *Scientific Drilling* 21, 29–40. https://doi.org/10.5194/sd-21-29-2016

Russell, J.M., Vogel, H., Bijaksana, S., Melles, M., Deino, A., Hafidz, A., Haffner, D., Hasberg, A.K.M., Morlock, M., von Rintelen, T., Sheppard, R., Stelbrink, B., Stevenson, J. (2020) The late quaternary tectonic, biogeochemical, and environmental evolution of ferruginous Lake Towuti, Indonesia. *Palaeogeography, Palaeoclimatology, Palaeoecology* 556, 109905. https://doi.org/10.1016/j.palaeo.2020.109905

Sekerci, F., Balci, N. (2022) Microbial Acid Sulfate Weathering of Basaltic Rocks: Implication for Enzymatic Reactions. *Aquatic Geochemistry* 28, 155–184. https://doi.org/10.1007/s10498-022-09407-8

Viollier, E., Inglett, P.W., Hunter, K., Roychoudhury, A.N., Van Cappellen, P. (2000) The ferrozine method revisited: Fe(II)/Fe(III) determination in natural waters. *Applied Geochemistry* 15, 785–790. https://doi.org/10.1016/S0883-2927(99)00097-9

Vuillemin, A., Friese, A., Alawi, M., Henny, C., Nomosatryo, S., Wagner, D., Crowe, S.A., Kallmeyer, J. (2016) Geomicrobiological Features of Ferruginous Sediments from Lake Towuti, Indonesia. *Frontiers in Microbiology* 7, 1007. https://doi.org/10.3389/fmicb.2016.01007

Vuillemin, A., Wirth, R., Kemnitz, H., Schleicher, A.M., Friese, A., Bauer, K.W., Simister, R., Nomosatryo, S., Ordoñez, L., Ariztegui, D., Henny, C., Crowe, S.A., Benning, L.G., Kallmeyer, J., Russell, J.M., Bijaksana, S., Vogel, H., the Towuti Drilling Project Science Team (2019a) Formation of diagenetic siderite in modern ferruginous sediments. *Geology* 47, 540–544. https://doi.org/10.1130/G46100.1

Vuillemin, A. Friese, A., Lücke, A., Bauer, K.W., Nomosatryo, S., Simister, R., Ordoñez, L.G., Ariztegui, D., Russell, J.M., Bijaksana, S., Vogel, H., Crowe, S.A., Kallmeyer, J., the Towuti Drilling Project Science Team (2019b) Pore water geochemistry and bulk sediment measurements of downcore profiles from site TDP-1A of the ICDP Towuti Drilling Project, Lake Towuti, Indonesia. *PANGAEA*. https://doi.pangaea.de/10.1594/PANGAEA.908080

Vuillemin, A., Mayr, C., Friese, A., Bauer, K.W., Lücke, A., Heuer, V.B., Glombitza, C., Henny, C., von Blanckenburg, F., Russell, J.M., Bijaksana, S., Vogel, H., Crowe, S.A., Kallmeyer, J. (2021) Siderite C-O-Fe isotope compositions, pore water geochemistry and bulk sediment parameters from the 100-m-long core TDP-1A of the ICDP Towuti Drilling Project, Lake Towuti, Indonesia. *PANGAEA*. https://doi.pangaea.de/10.1594/PANGAEA.934401

Vuillemin, A., Mayr, C., Schuessler, J.A., Friese, A., Bauer, K.W., Lücke, A., Heuer, V.B., Glombitza, C., Henny, C., von Blanckenburg, F., Russell, J.M., Bijaksana, S., Vogel, H., Crowe, S.A., Kallmeyer, J. (2023) A one-million-year isotope record from siderites formed in modern ferruginous sediments. *GSA Bulletin* 135, 504–522. https://doi.org/10.1130/B36211.1

Weltje, G.J., Tjallingii, R. (2008) Calibration of XRF core scanners for quantitative geochemical logging of sediment cores: Theory and application. *Earth and Planetary Science Letters* 274, 423–438. https://doi.org/10.1016/j.epsl.2008.07.054